BRNO UNIVERSITY OF TECHNOLOGY
VYSOKÉ UČENÍ TECHNICKÉ V BRNĚ

FACULTY OF MECHANICAL ENGINEERING
FAKULTA STROJNÍHO INŽENÝRSTVÍ

INSTITUTE OF PHYSICAL ENGINEERING
ÚSTAV FYZIKÁLNÍHO INŽENÝRSTVÍ

ELECTRON TWEEZER
ELEKTRONOVÁ PINZETA

MASTER'S THESIS
DIPLOMOVÁ PRÁCE

AUTHOR   Bc. MARTIN ŠTUBIAN
AUTOR PRÁCE

SUPERVISOR   Ing. PETR BÁBOR, Ph.D.
VEDOUCÍ PRÁCE

BRNO 2020

Specification Master's Thesis

Department:	Institute of Physical Engineering
Student:	**Bc. Martin Štubian**
Study programme:	Applied Sciences in Engineering
Study branch:	Physical Engineering and Nanotechnology
Supervisor:	**Ing. Petr Bábor, Ph.D.**
Academic year:	2019/20

Pursuant to Act no. 111/1998 concerning universities and the BUT study and examination rules, you have been assigned the following topic by the institute director Master's Thesis:

Electron tweezer

Concise characteristic of the task:

The Au–Ge and Au–Si alloys used in the production of nanowires by the VLS growth method can be moved over a sufficiently smooth and hot surface using an electron beam. This in the literature undescribed phenomenon was observed at the Institute of Physical Engineering recently. An electron beam with a controlled moving droplet can be called an electron tweezer. The mechanism of this movement is not yet fully understood. The aim of the diploma thesis will be to perform experiments and simulations that clarify the mechanism of the movement of the droplets and if possible, utilize this motion to create nanostructures.

Goals Master's Thesis:

1. Design and perform an experiment, including the preparation of appropriate samples, so that the movement of the droplets caused by the electron beam can be observed qualitatively under different experimental conditions.
2. Simulate the influence of the electron beam on the surface temperature surrounding the droplets.
3. If possible, try to use electron tweezers to create nanostructures.

Recommended bibliography:

RATH, A.; JULURI, R. R.; SATYAM, P. V. Real Time Nanoscale Structural Evaluation of Gold Structures on Si (100) Surface Using in-Situ Transmission Electron Microscopy. J. Appl. Phys. 2014, 115.

BÁBOR, P.; DUDA, R.; POLČÁK, J.; PRŮŠA, S.; POTOČEK, M.; VARGA, P.; ČECHAL, J.; ŠIKOLA, T. Real-Time Observation of Self-Limiting SiO_2/Si Decomposition Catalysed by Gold Silicide Droplets. RSC Adv. 2015, 5, 101726–101731.

FERRALIS, N.; GABALY, F. El; SCHMID, A. K.; MABOUDIAN, R.; CARRARO, C. Real-Time Observation of Reactive Spreading of Gold on Silicon. Phys. Rev. Lett. 2009, 103, 1–4.

Deadline for submission Master's Thesis is given by the Schedule of the Academic year 2019/20

In Brno,

L. S.

....

prof. RNDr. Tomáš Šikola, CSc.   doc. Ing. Jaroslav Katolický, Ph.D.
Director of the Institute   FME dean

Abstract

This work deals with a new way of manipulating micro and nano objects, specifically liquid AuGe islands by using an electron beam. In the first part, the mechanism of manipulation is discussed, the principle is described and then are shown experiments and simulations which are confirming this principle. The second part of the work deals with the use of this manipulation in fabrication of micro / nano structures.

Abstrakt

Táto práca sa zaoberá novým spôsobom manipulácie mikro a nano objektov, konkrétne tekutých AuGe ostrovčekov pomocou elektrónového zväzku. V prvej časti je diskutovaný mechanizmus manipulácie, je popísaný princíp a ďalej sú uvedené experimenty a simulácie potvrdzujúce tento princíp. Druhá časť práce sa zaoberá využitím uvedenej manipulácie k tvorenie mikro/nano štruktúr.

Keywords

Kľúčové slová

Reference

ŠTUBIAN, Martin. *Electron tweezer*. Brno, 2020. Master's thesis. Brno University of Technology, Faculty of Mechanical Engineering. Supervisor Ing. Petr Bábor, Ph.D.

Electron tweezer

Declaration

I declare that I have developed this master's thesis independently under the guidance of Ing.Petr Bábor, Ph.D.. I listed all the literary sources, publications and other sources from which I drew.

. . . .

Martin Štubian

June 23, 2020

Acknowledgements

Contents

Chapter 1

Introduction

The name of this thesis is electron tweezers. The reason why such a name was chosen is that it is possible to manipulate liquid metallic islands by using the electron beam near them. In this fashion, it is a little similar to the well known optical tweezers that use highly focused laser beam [1] to manipulate with the micro-objects. By using an electron beam induced temperature gradient it is possible to manipulate with the mentioned liquid metallic islands, which are forced to migrate in the direction of the temperature gradient. The diameters of these islands are ranging from hundreds of nanometers up to units of millimeters.

As it is often very difficult or in many cases nearly impossible, to manipulate with objects of the micro world, this mechanism could prove to be a very useful tool in many scientific fields (e.g. micro-electronics). As will be presented in the thesis it is possible to combine the controlled manipulation with other mechanisms (such as vapor-liquid-solid growth method) to create new possibilities in the respective fields.

Although, the migration of two-component liquids in the temperature gradient is not anything new in the scientific world, there are still many disagreements between theoretical models and experiments. This is due to the very complicated nature of mass and heat transport phenomenons that are occurring during the migration.

Also, the electron beam induced migration of the liquid metallic islands is not a new discovery (it was reported by Ichinokawa et al. [2] in 1993), however, there are very few studies published on this phenomenon. With the ever-increasing capabilities of scientific instruments (in my work I mainly used two „high-end" UHV SEMs shown in section 3.2.1) it was possible to study this phenomenon in detail as well as combine it with some other processes in order to find some practical application.

Chapter 2

Theoretical introduction to migration of liquid eutectic alloys

The phenomenon of externally induced mass transport in liquid eutectic alloy islands (droplets) plays a major role in this thesis. This phenomenon has been known for quite some time and has been thoroughly investigated. The driving force of this mass transport is mainly concentration gradient induced in the islands by the temperature gradient, this is discussed in section 2.2. Additionally, also thermomigration effect may play a role in this mass transport, and in the presence of the electric currents, also electromigration effect occurs. As these effects are rather complicated, they are discussed in detail in the following section 2.1.

2.1 Electromigration and thermomigration

2.1.1 Electromigration

The electromigration is electric field-induced transport of mass. The phenomenon is very general and can be observed in solids, liquids, and gases. It is particularly important in the field of microelectronics, as it is closely related to the circuit reliability [3]. With the introduction of the first integrated circuits (ICs) in the late 1960s, the electro-migration became a thoroughly investigated effect, as it was the main cause of the very short life span of the new ICs. As previously mentioned, the vast majority of research is connected to the microelectronics, namely the electromigration in metals. This section will use that to provide insight into the topic of electromigration.

The source for this section is mostly [3]. Atoms in a solid move by the process of diffusion. In most cases, the diffusive movement of atoms is occurring by exchange with neighboring vacancies (see Fig. 2.1a). When the driving force is applied, the direction of diffusion is biased in the direction of the driving force (see Fig. 2.1b). That leads to a net flow of atoms in that direction. When an electric field $\mathbf{E}$ is applied to a material, resultant changes in the internal local electric field lead to net forces on the atoms. According to [4] for small electric fields $\mathbf{E}$, a linear expression for the force $\mathbf{F}_{el}$ is written as

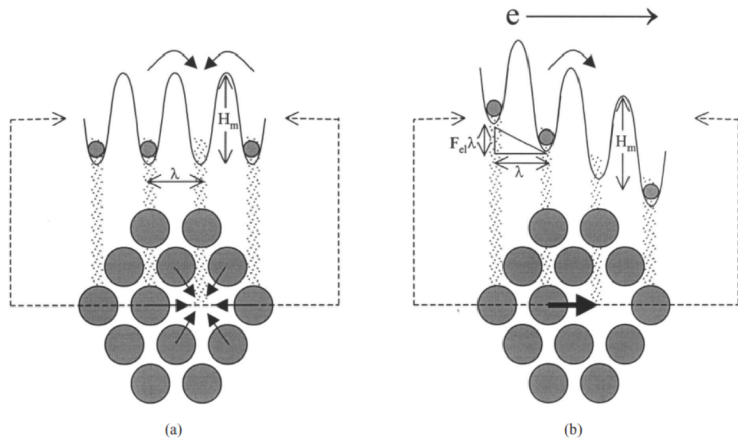$$\mathbf{F}_{el} = |e|z^*\mathbf{E}, \tag{2.1}$$

4

Figure 2.1: Schematics of diffusion of atom in a 2D hexagonal lattice. a): Without a driving force. All of the neighboring atoms are equally likely to switch places with the vacancy. b): The atom placed to the left of the vacancy switches preferentially with the vacancy, due to the flow of electrons. λ is lattice constant and H_m is the height of the energetic barrier. Taken from [3].

where e is the electric charge and z^* is the effective valence, which by convention expresses the magnitude and direction of the force. For most metals, z^* is negative, which means that atoms move against the electric field or in the direction of electron flow.

The interaction of the local electric field and the electrons with the atom is usually divided into two components. One component is the direct electrostatic force between the ions in the solid and the applied electric field. This force is generally argued to be small due to the efficient electron screening. The second component which dominates in metals is the electron wind force. This force arises from momentum transfer by conduction electrons scattering with the ions in the solid and effectively pushes the ions in the direction of the electron flow.

For sufficiently small driving forces ($F_{el} \cdot \lambda \ll H_m$, where λ is lattice and H_m is the height of the energetic barrier (see Fig. 2.1)), the effect of the electric field on atom motion can be viewed as a small perturbation on the usual diffusion process. In a pure system, the net flux of atoms $\mathbf{J}$ is given by Nernst-Einstein relation

$$\mathbf{J} = \frac{cD}{kT}\mathbf{F}_{el} = \frac{cD}{kT}ez^*\mathbf{E}, \qquad (2.2)$$

where c is the atom concentration, D is the self-diffusion coefficient, k is Boltzmann's constant, T is the absolute temperature. By using Ohm's law ($\mathbf{E} = \rho\mathbf{j}$) the equation (2.2) can be written as

$$\mathbf{J} = \frac{cD}{kT}ez^*\rho\mathbf{j}, \qquad (2.3)$$

where ρ is the metal resistivity, and $\mathbf{j}$ is the current density (not to be confused with $\mathbf{J}$ which is atom flux). Thus trough the applied electric field, an electromigration flux is generated.

Furthermore, we can expand the diffusion coefficient D by using the Arrhenius equation and divide equation (2.3) by atom concentration ($v = \mathbf{J}/c$), in order to get the average drift velocity of migrating atoms. By doing this we get

$$\mathbf{v} = \frac{D_0}{kT} e z^* \rho \mathbf{j} \exp\left(-\frac{\Delta H}{kT}\right), \tag{2.4}$$

where D_0 is the diffusion constant and ΔH is the activation energy. It is often convenient to rewrite equation (2.4) in the form

$$\frac{\mathbf{v}T}{\mathbf{j}} = \frac{D_0 e z^* \rho}{k} \exp\left(-\frac{\Delta H}{kT}\right). \tag{2.5}$$

Equation (2.5) can be used to obtain the activation energy ΔH and the preexponential factor (diffusion constant) from the usual Arrhenius plot.

It is important to note that this simple picture holds true only in simple and pure metals, in which the wind force dominates. If the impurities are present, this simple picture breaks down. For instance, when impurities diffuse by a vacancy mechanism, there is a coupling between the host and impurity, and z^* and D can no longer be separated [5].

According to the conservation of matter, a divergence in the electromigration atom flux will lead to atom accumulation or depletion. This will eventually cause damage to the interconnections in ICs. In the case of liquid eutectic islands, this causes the concentration gradient in the island and as a result, the island moves. One such case is shown in Figure 2.2. The direction of electromigration depends on the material of the island.
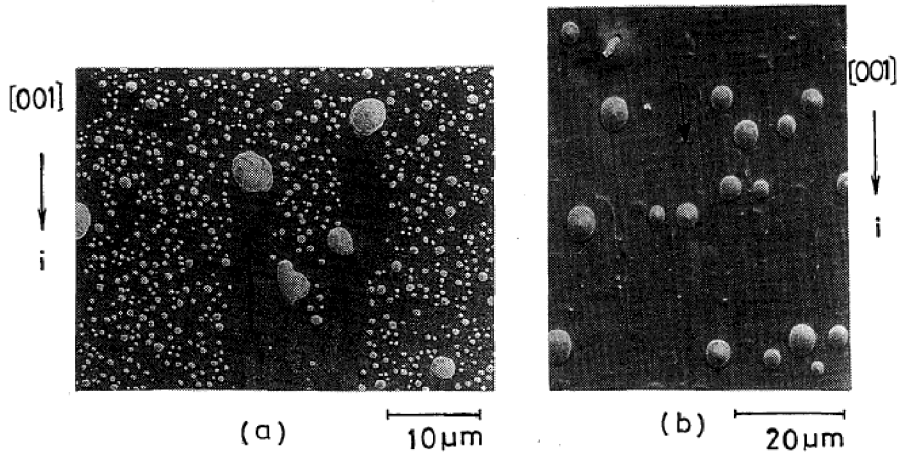

Figure 2.2: a) Electromigration of AuSi islands and b) of AlSi islands. Note that AuSi islands move against the direction of the current, while AlSi islands migrate along the direction of the current. Taken from [2].

6

2.1.2 Thermomigration

Similarly to the electromigration also the temperature gradient across the material can cause migration of atoms this is regarded as thermomigration also known as Soret effect or thermophoresis. Thermomigration can be observed at the scale of one millimeter or less. This phenomenon was first observed by John Tyndall in 1870 and was further researched and understood by Charles Soret in 1879, who studied the thermomigration in liquid mixtures.

Thermomigration has numerous practical applications. The basis for these applications is the difference in forces that are applied trough the temperature gradient. This can be exploited to separate the particle types after they have been mixed or keep them from mixing if they are separated. The thermophoretic force has been used in commercial precipitators and is also being used in the production of optical fibers during the vacuum deposition process. It is also used in microbiology for manipulating single biological macromolecules, such as DNA [6]. Furthermore, it is often encountered, similarly as the electromigration, in the field of electronics, e. g. the thermomigration in solder joints [7].

Additionally, thermomigration in flip-chip solder joints may also occur as a consequence of the previous electromigration. [8]. It is because of Joule heating, the electromigration causes non-uniform temperature distribution. Due to the current crowding, the chip side of the flip-chip solder joint is hotter than the substrate side and thus a thermomigration can occur [9].

Fundamentally, thermomigration is a cross effect or interaction between mass flow and heat flow. Therefore, from the theoretical point of view, thermomigration is an effect of irreversible thermodynamics [10]. In order to provide some insight into the theory, few results of [11] is presented in the following section. [11] is an attempt of an atomistic interpretation of thermomigration and develops the phenomenological equations from irreversible thermodynamics.

In the case of two-component alloy which has been held for a long time in a temperature gradient if a system reaches time-independent concentration gradient ∇c, then the generalized forces acting upon atoms, which arise from concentration ($F_c = kT\nabla \ln c$) and temperature ($F_A = Q\nabla \ln T$) gradient, will be equal. Then we can write

$$- kT\nabla \ln c = Q_m \nabla \ln T, \tag{2.6}$$

where the quantity Q_m is a measure of the thermomigration and is called *measured heat of transport*.

In the case of a pure metal, the time-independent flux of matter is usually measured. The flux of matter, when the vacancy mechanism takes place, is the negative of the flux of vacancies ($\mathbf{J}_v = -\mathbf{J}_1$). The flux of matter will be then given by

$$- \frac{kT\gamma}{c_1 D_1}\mathbf{J}_1 = Q'_m \nabla \ln T, \tag{2.7}$$

where again the quantity Q'_m measures the thermomigration of the material component, D_1 is the tracer diffusivity, c_1 is the atom concentration of the pure component 1 and γ is the correlation coefficient for different lattices. [11] contains a table for the

Q'_m for some pure solid metals, interstitial solid solutions, and binary substitutional solid solutions.

Similarly, as in the electromigration (equation (2.4)), the diffusion coefficient D_1 is expanded by Arrhenius equation and the flux $\mathbf{J}_1$ is divided by the atom concentration c_1. Then, one can rewrite equation (2.7) in the following form

$$\mathbf{v} = -\frac{D_0 Q'_m}{kT^2} \nabla T \exp\left(-\frac{\Delta H}{kT}\right) \tag{2.8}$$

Once again one can construct Arrhenius plot from velocities in order to get activation energy ΔH and diffusion constant D_0.

Finally, it is clear that the direction of thermomigration is determined by a sign of Q'_m. A positive sign means that atoms migrate towards the colder region (against the direction of temperature gradient) and vice versa. In Figure 2.3 are shown migrating AuSi islands in the temperature gradient. [2] says the main mechanism behind this migration is thermomigration, however that might not be the case as will be shown below (section 2.2).
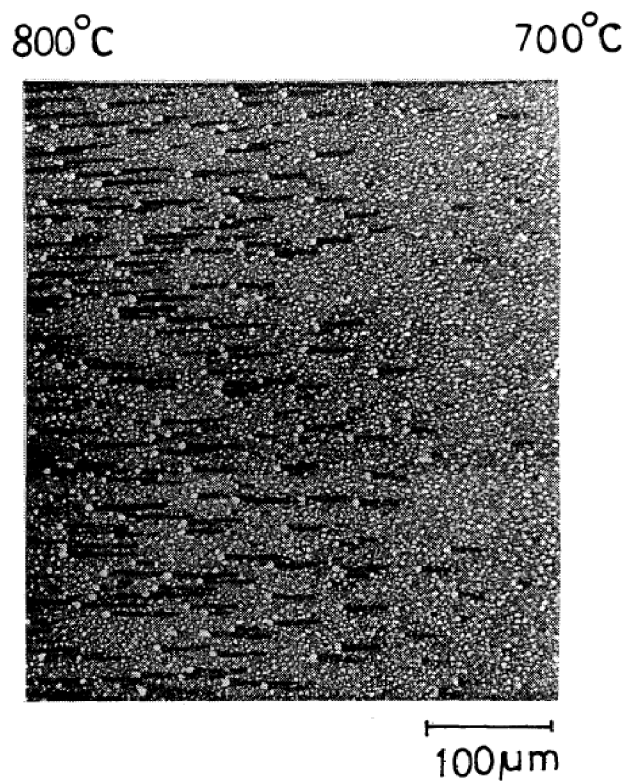

Figure 2.3: Migration of liquid AuSi islands in temperature gradient. Islands are migrating from the cold side to the hot side Taken from [2].

8

2.2 Migration of liquid metallic islands in a temperature gradient

Even though the previous description of the theory was for an atomic scale, [2] says that thermo and electromigration also happen on larger scales, namely thermo and electromigration of liquid metallic islands and uses equation (2.8) to determine activation energies of thermomigration. It is important to distinguish between these cases in the usage of term thermo/electromigration. To avoid confusion term migration will be associated with the movement of the liquid islands and term thermomigration shall be associated with the diffusion processes in the island. Indeed, these systems are fundamentally different (previous sections described migration in solid metals, although [2] uses these equations also for liquid metallic islands) from ones described in the previous sections. One must proceed with caution while trying to apply previous theories for these specific cases.

In the case of electromigration, the situation is much simpler than in the presence of a temperature gradient. Due to the absence of temperature gradient one can be sure that the driving force behind the migration of liquid islands is the electric current or more specifically the electromigration, however, in a temperature gradient situation becomes more complicated as more effects come into place and effects such as thermomigration may not be dominant driving forces and indeed in the literature, it is in many cases not even taken into consideration.

In the literature, the migration of liquid metallic islands in a temperature gradient is explained as follows. The migration is caused by the dissolution of atoms of the solid on the hot face of the island, diffusion of the dissolved atoms across the island, and the subsequent deposition of the dissolved atoms of the solid on the cold side of the island [12][13] (see Fig.2.4). This simplest mechanism is also explained in Figure 2.5 via the phase diagrams of Au-Ge system.
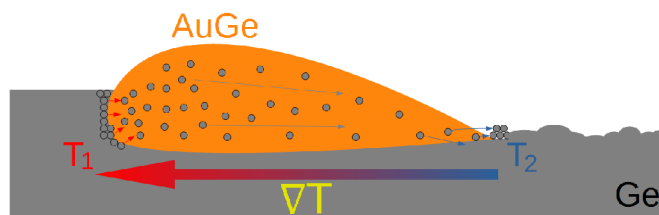

Figure 2.4: Schematic of migrating AuGe liquid island due to the temperature gradient $T_1 > T_2$. Atoms on the hotter face dissolve into the liquid diffuse across the island and deposit on the cold face.

However, [2] says, that also electro and thermomigration of metal atoms against host atoms (in our case Au against Ge) across the solid-liquid interface occurs. This will be discussed below.
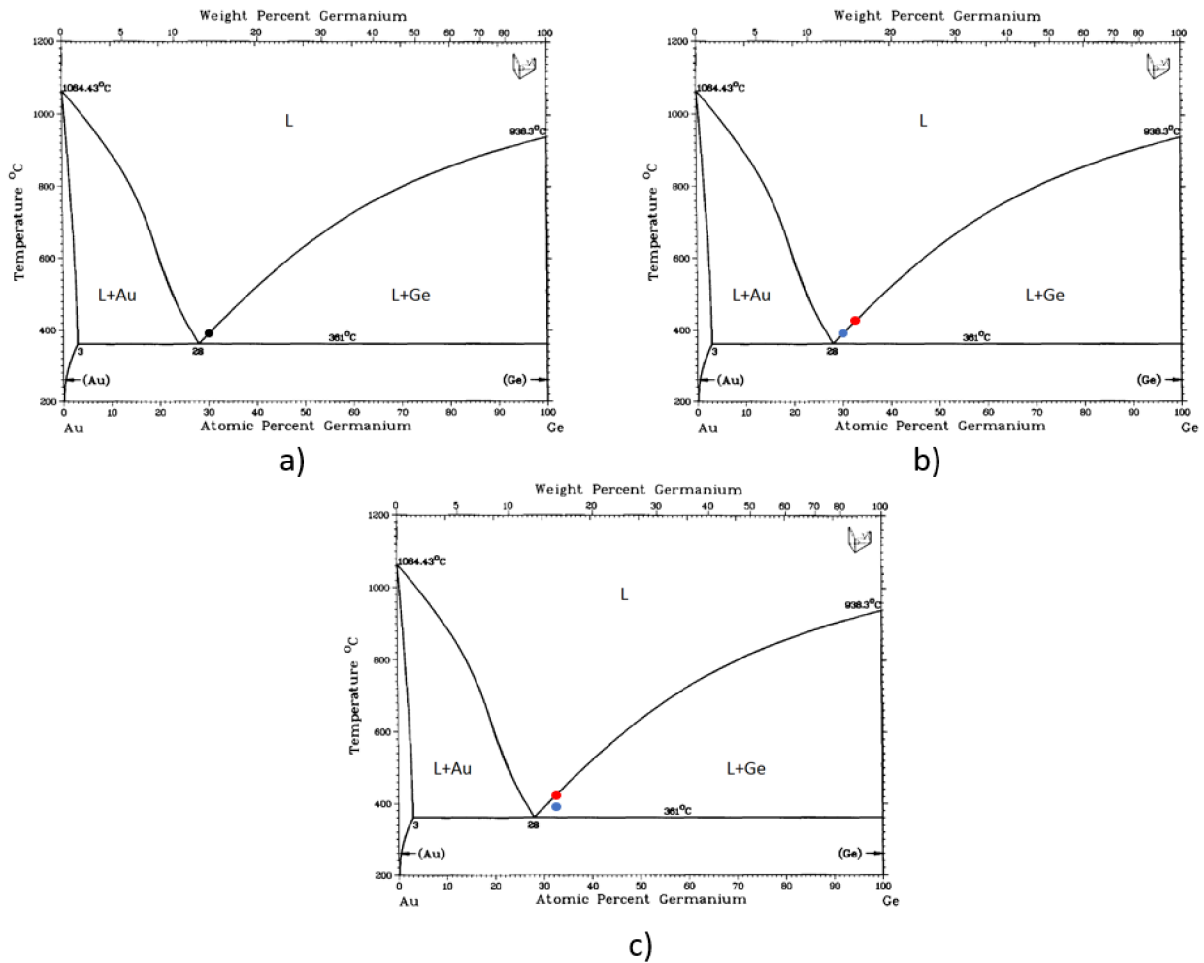
Figure 2.5: Mechanism of migration of liquid metallic islands in a temperature gradient. a) Island composition marked by a black dot is in equilibrium state at the temperature 400°C. b) By increasing the temperature by 40°C on one face (marked by a red dot) will this side start dissolving more Ge atoms and its composition will be changed, while on the cold side composition remains unchanged (marked by a blue dot). This creates a concentration gradient from the hot face to the cold face. c) Ge atoms diffuse to the cold face. This face is artificially pushed to the non-equilibrium state by the concentration gradient. Due to the non-equilibrium state, the cold face will start to deposit the Ge atoms.

Migration is a combination of all effects running simultaneously. The hot face „wants" more Ge atoms, and thus moves, while dissolved atoms are diffusing to the cold face, where they are being deposited out of the island. Phase diagrams are taken from [14].

10

2.2.1 Migration of large AuSi islands

Here shall be discussed a case of migration of large AuSi islands (diameters of units of mm) on the Si surface in the temperature gradient [15]. It is expected, due to the large island sizes and relatively high temperature gradient (50°C/cm), that the effect of interface kinetics on the island velocity is small [16]. The velocity $\mathbf{V}$ of an island can be then determined from the silicon mass balance equation at the forward or rear face of the island as

$$\mathbf{V} = -\frac{\mathbf{J}_L}{C_S}, \tag{2.9}$$

where $\mathbf{J}_L$ is the flux of silicon across the AuSi island and C_S is the concentration of Si in solid silicon. If the thermomigration effect is ignored in the liquid Au-Si system, the flux of Si $\mathbf{J}_L$ is according to Fick's law

$$\mathbf{J}_L = -D\nabla C_L, \tag{2.10}$$

where D is the diffusion coefficient of silicon in the island and ∇C_L is the concentration gradient across the droplet. Since concentration depends on the temperature one can write

$$\nabla C_L = \left(\frac{\partial C}{\partial T}\right)\nabla T_L,$$

where $\partial C/\partial T$ can be taken from the phase diagram of the Au-Si system and ∇T_L if the temperature gradient in the droplet liquid. The thermal conductivities of the liquid and solid are approximately equal (justification is also in [15]), then $\nabla T_L = \nabla T_S$. Combining equations (2.9) and (2.10), one finds the island velocity as

$$\mathbf{V} = \frac{D^*}{C_S}\frac{\partial C}{\partial T}\nabla T_S, \tag{2.11}$$

where the effect of interface kinetics, thermal conductivity, and thermomigration are assumed to be small and are incorporated in an approximate effective diffusion coefficient D^*.

2.2.2 Effects of thermomigration and interface kinetics

This section uses [12], which utilized brine (high concentration solution of salt, i.e KCl, in water) islands on solid KCl (potassium chloride) to investigate the migration of liquid islands trough solids. Once again starting point is the mass-balance equation at the interface

$$\mathbf{V} = -\frac{\mathbf{J}}{C_S}, \tag{2.12}$$

where $\mathbf{J}$ is the normal flux of KCl impinging on the interface and C_S is the molar concentration of KCl in the solid. The flux of KCl is generated by the concentration gradient ∇C_l (as in the previous section 2.2.1) and the temperature gradient ∇T in the liquid normal to the interface. The flux has then form

$$\mathbf{J} = -D(\nabla C_L + \sigma C_L \nabla T), \tag{2.13}$$

where D is the diffusion coefficient of KCl in brine, C_L is the concentration of KCl in brine and σ is the Soret coefficient, which is defined as the ratio of the thermal diffusion coefficient D_T to the ordinary diffusion coefficient D [17] ($\sigma = D_T/D$). Soret coefficient expresses the relation between the mass flow and heat flow. The concentration of KCl in the liquid at the ith face of a migrating island depends on four factors:

1. The solubility of solid KCl at interface temperature of the ith facet.

2. The change in solubility of solid KCl caused by the „effective curvature" of the ith facet [18].

3. The supersaturation or undersaturation, which is needed to cause interface migration of the ith facet [16].

4. The change in KCl concentration caused by thermomigration. This is already explicitly incorporated in equation (2.13).

[12] then investigates the influence of the first three factors using chemical potentials in the solid and in the liquid and also assuming mechanical equilibrium at the ith facet, and finds steady-state state velocity of migrating island as

$$\mathbf{V} = D \frac{C_l}{C_s} \left[\left(\frac{1}{C_E} \frac{\partial C_E}{\partial T} + \sigma \right) \nabla T_l - \frac{K_D + K_S}{(RT)L} \right], \tag{2.14}$$

where D is the diffusion coefficient of KCl in the brine, C_l is the average concentration of KCl in the brine island, C_E is the equilibrium solubility of KCl in brine, R is the gas constant, and L is thickness of the island. Moreover, K_D/K_S is the change in chemical potential at the solid-liquid interface of the ith facet generated by irreversible processes associated with the transfer of KCl atoms between the solid and liquid phases, $K(i)$ has form

$$\mu_l(i) = \mu_s(i) - K(i), \tag{2.15}$$

where $\mu_{l/s}(i)$ are the chemical potentials of KCl in the liquid/solid. For a dissolving facet $K = K_D$ and for a depositing facet $K = -K_S$. This is simply an expression of the idea that for deposition and dissolution to happen at the interface, the chemical potential of the host material (KCl, Si, or Ge) in the liquid must be higher and lower, respectively, than the chemical potential of the host material in the solid.

Additionally, the temperature gradient in the liquid island ∇T_l, will vary with the island shape and dimensions, if the thermal conductivities of the solid and liquid are not equal. The second term in equation (2.14) expresses the effects of interface kinetics. With the decreasing island size, the effects of interface kinetics will increase and below the critical size of the island, there will be no island migration. This corresponds well with the observations that have been made in our experiments, where smaller islands did not move. The effects of thermomigration are in Soret coefficient σ, whether the thermomigration enhances the migration of islands or on the contrary acts against it is determined by the sign of σ. Moreover, if one ignores the

interface kinetics (second term) and the effects of thermomigration equation (2.14) acquires a form of equation (2.11).

Naturally, the theory of this particular subject is very complicated and there are many discrepancies between the theory and experimental observations. [12] itself discuses some of these discrepancies. However, this description highlights the basic ideas behind the mechanism of migration and predicts its properties, which were also observed during my experiments.

2.3 Migration of liquid droplets without mass transport mechanisms

At the end of the theoretical introduction to liquid island migration, yet another mechanism of migration is introduced. This mechanism is not necessarily involved in the migration of the AuGe islands on the germanium substrate, because there is no mass transport involved. In the previous mechanisms, mass transport was the main reason behind the island migration. However, this mechanism occurs for any liquid on the gradient surface (note that term droplet was used in the title, rather than an island). It is fundamentally different from the previous mechanisms as it is derived from hydrodynamics, namely the lubrication theory. Naturally, one could ask why this mechanism is introduced, when it is not involved in the migration of AuGe islands. The answer is rather simple, it is because of its importance in future experiments that may follow this thesis. For example, if one could fabricate AuGe liquid islands on the surface that does not interact with the island, islands could still migrate on the surface via this mechanism. In fact, there was an attempt to fabricate AuGe islands on the graphene surface to study this mechanism, however, due to the technical difficulties was this experiment dropped (see section 3.2.1). Another advantage is that this mechanism occurs for any liquid when the right conditions are met. So in principle, one could control the migration of any liquid via an electron beam induced temperature gradient. In this section, the basic mechanism is presented.

The motion of liquid droplets on the solid horizontal surfaces has been long known phenomenon (e.g. [19]). In 1989 F. Brochard-Wyart published a theoretical study of a 1-D liquid droplet placed on the horizontal gradient surface [20]. Moreover many experimental studies has been conducted on this particular phenomenon (e.g. [21][22][23]). In this chapter, a summary of thesis related cases of Brochard's study is presented. Motion occurs when either (i) chemical gradient (e.g. PH gradient) or (ii) temperature gradient is induced on the surface. For this work only the temperature gradient induced motion is important, therefore only this case will be discussed. Additionally, only cases with negligible effects of gravity and droplets with partial wetting, where the spreading coefficient is positive, will be presented. Spreading coefficient S is defined as:

$$S = \gamma_{SG} - (\gamma_{SL} + \gamma) \tag{2.16}$$

Where $\gamma_{SG/SL}$ are respectively solid-gas / solid-liquid surface tensions and γ is the liquid-gas surface tension (free surface tension).

Since the liquid/vapor surface tension γ is temperature dependent, the temperature gradient ∇T induces surface tension gradient $\nabla\gamma$. Surface tension gradient induces a Marangoni flow [24] (the detailed mathematical study of the Marangoni effect can be found in [25]) in the droplet.

The motion of the droplets on the surfaces with the temperature gradient is a combination of Marangoni flow (driven by the $\gamma(T)$) and solid-driven flow (driven by $\gamma_{SG}(T) - \gamma_{SL}(T)$). For small gradients the two terms are additive. While hydrodynamical equations combining all effects are very complex, [20] uses two simplifications (i) solutions describing static droplet are known [26], (ii) applied gradients are small ($\nabla T \to 0$), the droplet shape is only weakly affected by the flow. Additionally, [20] considers only nonvolatile liquids, avoiding any wetting process trough a vapor phase.

The calculation of velocity for an one-dimensional geometry of the droplet (shown in figure 2.6) is done by balancing 1) <u>capillary forces</u> and 2) <u>viscous forces</u>.
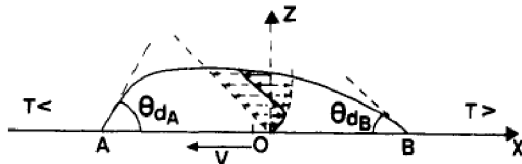

Figure 2.6: Moving 1-D liquid droplet on a surface with temperature gradient. $\theta_{d_{A/B}}$ are dynamic contact angles in colder resp. hotter region. V is velocity of the moving droplet. Taken from [20].

1. **Capilary force** (i.e. mechanical force) with which the solid acts on the liquid droplet is given as:

$$F_d = (\gamma_{SG} - \gamma_{SL})_B - (\gamma_{SG} - \gamma_{SL})_A = (S' + \gamma')l \qquad (2.17)$$

   where l is the length of the droplet, $S' = \frac{dS}{dx} = \frac{dS}{dT}\frac{dT}{dx}$ and $\gamma' = \frac{d\gamma}{dx} = \frac{d\gamma}{dT}\frac{dT}{dx}$. Note that this force depends only on the size of the droplet, temperature gradient and materials of the solid surface, droplet, and surrounding atmosphere.

2. **Viscous force** is much more complex, therefore its calculation is not shown here. It uses lubrication approximation [27], where the liquid flow is the superposition of a Poiseuille flow induced by the pressure gradient $\frac{\partial P}{\partial x}$ and a simple shear flow induced by the the stress $\frac{\partial \gamma}{\partial x}$ at the free surface. The total viscous force with which the droplet acts on the solid surface is:

$$F_v = \int_A^B 3\eta\frac{V}{\zeta}dx - \frac{1}{2}(\gamma_B - \gamma_A) \qquad (2.18)$$

   where η is the viscosity of the droplet, $\zeta(x)$ is the function of droplet thickness and $\gamma_{A/B}$ is the liquid-gas surface tension at the droplets borders (see figure 2.6). The second term in equation (2.18) is contribution from the Marangoni flow.

Equation (2.18) is valid for any droplet shape defined by the thickness function $\zeta(x)$. The droplet that has static shape part of a circle with a contact angle $\theta_e(0)$ (the equilibrium angle at the midpoint) we can write viscous force as:

$$F_v = 6\eta \frac{V}{\theta_e(0)} l_n - \frac{1}{2}\gamma' l \tag{2.19}$$

From the equality $F_d = F_v$, we get:

$$6\eta \frac{V}{\theta_e(0)} l_n = \left(S' + \frac{3}{2}\gamma'\right) l \tag{2.20}$$

where l_n is constant prefactor and is related to the macroscopic cutoff (size of the droplet) and molecular size. One can write equation (2.20) also as:

$$\eta V = \frac{2h_0}{3\eta l_n}\left(\frac{d}{dT}(\gamma_{SG} - \gamma_{SL}) + \frac{1}{2}\frac{d\gamma}{dT}\right)\frac{dT}{dx} \tag{2.21}$$

where h_0 is thickness of the droplet at the center. The first term in the bracket are the capillary forces while the second term is the contribution from the Marangoni flow. These two effects mean that the droplet can move to both directions (i.e. towards hotter region resp. colder region). Direction of the movement will then depend on the materials.

Chapter 3

Electron beam induced island migration

Ichinokawa et al. [2] reported in his research of electro and thermomigration of liquid eutectic metallic islands that island migration can be also induced by an electron beam. This phenomenon was also observed in my bachelor thesis [28], where migration of AuSi/AuGe liquid islands induced by the electron beam was observed (see Figure 3.1). It was decided to further study this phenomenon. By theoretical research
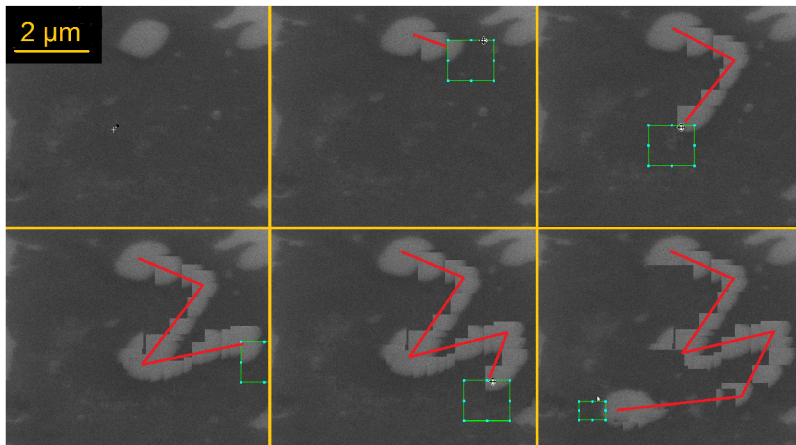

Figure 3.1: SEM image of a migrating AuSi liquid island. The green rectangle is a window where an electron beam is scanning, the island follows a reduced scanning window. The red line shows the islands' trajectory. Taken from [28].

(section 2), the mechanism of migration was determined. However, as Ichinokawa did not research this phenomenon thoroughly, and practically no other literature can be found on this particular occurrence, I studied the interaction of the electron beam and the liquid islands in more detail. The results are presented in this section. First, the interaction of the electron beam with a substrate was simulated, and the output of the simulation was energy distribution in the substrate. This energy distribution was then used as the input to another simulation which simulated heat distribution on the substrate and the output was a temperature field around the electron beam.

Then a combination of an experiment and the results of simulations was used to roughly estimate the needed temperature gradient for islands to move.

3.1 Simulations

3.1.1 Simulation of temperature field of a sample heated by direct current

In the experiments, the samples were always heated by direct current (DC). To get an insight, how does the temperature field look like on the surface of the sample simulation in Comsol Multiphysics® software [29] was made. It is very important to note that this is just a simulation to get an insight and the results are not used anywhere in later experiments or calculations. Comsol software uses a finite element method to solve various physics problems. This simulation was also done to see, whether an inconsiderable temperature gradient could be present on the surface because in the case of very large AuGe islands (diameter of hundreds of μm) spontaneous migration was observed (spontaneous in a sense that islands were not migrating under the influence of the electron beam).

The geometry of the simulated sample is shown in Figure 3.2. The material of the wires is tungsten with the diameter of 0.4 mm, which roughly corresponds to the diameter of tungsten wires that were used to hold samples and also provide connections to the heating current source. Dimensions of the simulated sample are $10 \times 2 \times 0.5$ mm^3 and the sample material is Ge(100). Values for material properties were predefined by Comsol. The surface emissivity coefficient for germanium was not predefined, thus value 0.55 [30] was used. Additionally, the conductivity of germanium was also not predefined and thus had to be estimated.
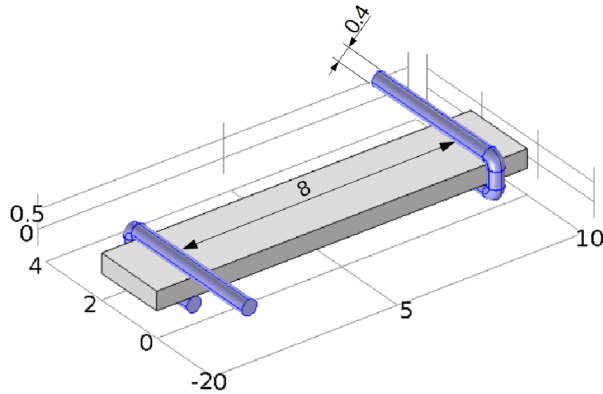

Figure 3.2: Geometry of the simulation. Tungsten wires are highlighted by blue color, while the gray block is the germanium sample. Scale is in mm.

In the experiments, samples were in a UHV chamber, therefore in the simulation, an assumption was made, that heat losses are occurring only via the radiation from the sample surface and heat that is dissipated by wires. For this reason, the length
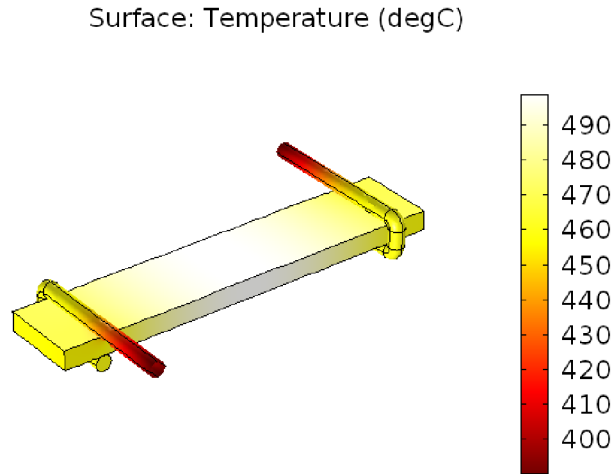
Surface: Temperature (degC)

Figure 3.3: Temperature field on the surface of the sample resulting from the simulation with the current set to 0.5 A. Dimension scale is in mm and temperature scale is in °C.
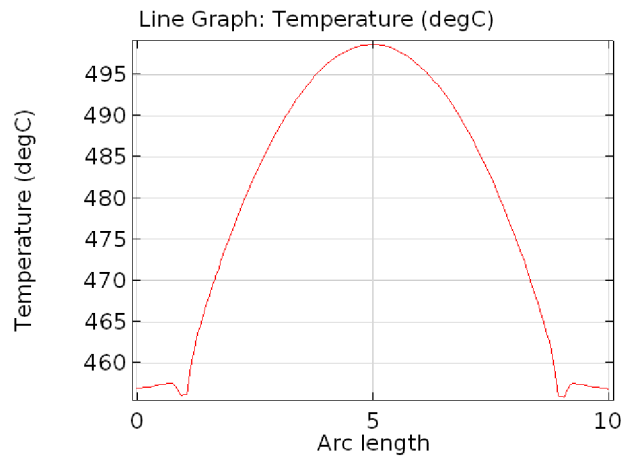

Figure 3.4: Cross section of the surface temperature field.

of the tungsten wires was set to 15 mm (this length is not shown in Figure 3.2) and the temperature at the end of wires was set to 100 °C. This setting and as well as the conductivity. Estimation was set so that the temperature corresponds to temperature measurements done by Radek Dao [31]. Radek measured temperature 497 °C with the current 0.5 A. This current value was also a typical value in the experiments where migration was observed. The result of the temperature field simulation is in Figure 3.3. The cross-section of the surface temperature field of the sample is in Figure 3.4. With the heating current set to 0.5 A, islands were liquid and migration was observed. This temperature is well above the eutectic point of the Au-Ge system, which is around 361 °C [14].

18

From Figures 3.3 and 3.4 it is clear that some temperature gradient could be present. If one approximates half of the line shown in Figure 3.4 with the straight line, the temperature gradient yielded by the simulation will be $7.6 \cdot 10^{-3}$ °C/μm. For the islands of diameters of hundreds of nm and units of μm the temperature gradient will be negligible, as this temperature gradient is not sufficient to induce the migration of islands of these diameters. However, it is important to note that with increasing current the temperature gradient also increases. It is unclear, whether this temperature gradient could be sufficient to cause migration of large islands (diameters of hundreds of μm) or this migration is caused by the current itself, and thus the electromigration. Fact that direction of migration of these large islands depends on the direction of the heating current favors the hypothesis that this migration is caused by electromigration, nevertheless, the spontaneous migration of large islands is not subject of this thesis, therefore it won't be discussed any further. An important output of this simulation is that some temperature gradient may be present due to the current heating, however for islands of smaller diameters it should not play a significant role.

3.1.2 Simulation of interaction of an electron beam with a germanium substrate

For the simulation of electron trajectories and their energy distribution Casino [32] software has been used. Casino uses Monte Carlo method to simulate electron trajectories and numerous other properties such as energy distribution of transmitted electrons, cathodoluminescence, and more.
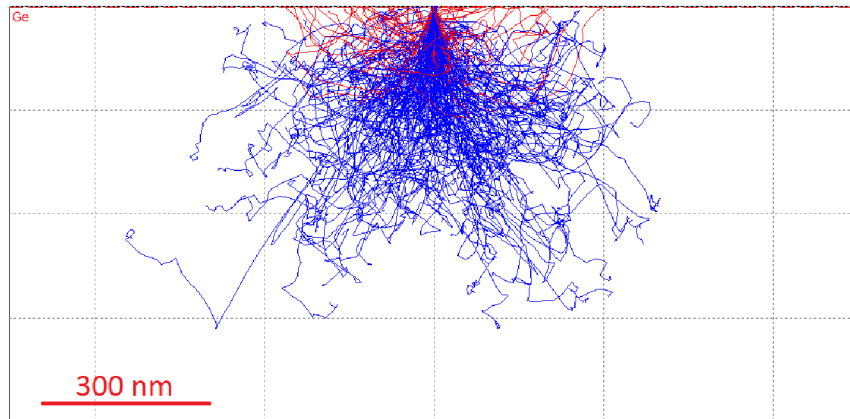

Figure 3.5: Simulated trajectories of 10 keV electron beam in the Germanium substrate. The blue are transmitted electrons, while red are the backscattered electrons.

For the simulation of the temperature field induced by the electron beam, the energy distribution is the most important quantity. In the simulation, an electron beam of energy 10 keV with the 5 nm spot size was used. The 10 keV energy electron beam was mostly used and island migration was observed with the beam of this energy. In Figure 3.5 are shown simulated electron trajectories of 10 keV electron
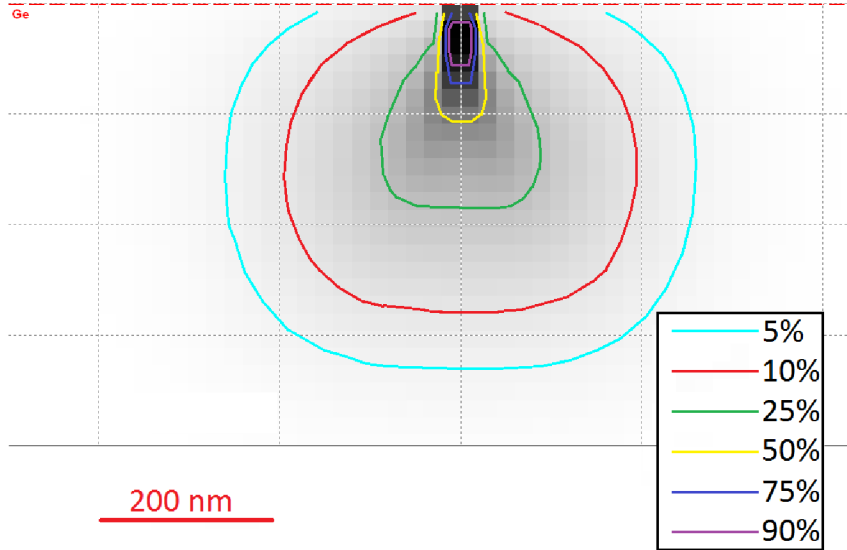
Figure 3.6: Energy distribution of the 10 keV electron beam in the Germanium substrate. The legend says how much energy is contained in the marked area. It is clear that most of the energy is contained in the purple marked area.

beam of 5 nm spot size in the Germanium substrate. In Figure 3.6 is shown the distribution of energy of electrons that were not backscattered. From Figure 3.6 it is apparent that most of the incoming energy (90%) is located in the area encircled by the purple line. This area has been used as the input for the next simulation of temperature field on the surface, which is shown in the following section 3.1.3.

3.1.3 Simulation of temperature field induced by the electron beam

Simulation of temperature field was done in Comsol Multiphysics® software [29]. In this case, a heat transfer in solids module was used. The result of the previous simulation of energy distribution in Casino was used as the power source in this simulation of heat transfer. First, it was needed to design a substrate. For this a simple $20 \times 20 \times 10$ μm^3 block (shown in Figure 3.7) was designed. Then material properties of Ge(100) were assigned to this block. Predefined values by Comsol were used for material properties (such as thermal conductivity, heat capacity and density). The energy distribution simulated in Casino was used to design a power source (shown in Figure 3.8) in a germanium substrate. According to [33] 40-80% of electron energy is converted to the heat in a sample. In the simulation, an 80% electron energy to heat conversion was assumed. With this, one can set the power for the power source as

$$P = U \cdot I \cdot 0.8, \tag{3.1}$$

where U is the accelerating voltage, which is in this case 10 kV, I is the electron beam current, and 0.8 is for energy conversion. Furthermore, the upper part of the source is set to contain 90% of the power, while the lower part is set to contain 10%
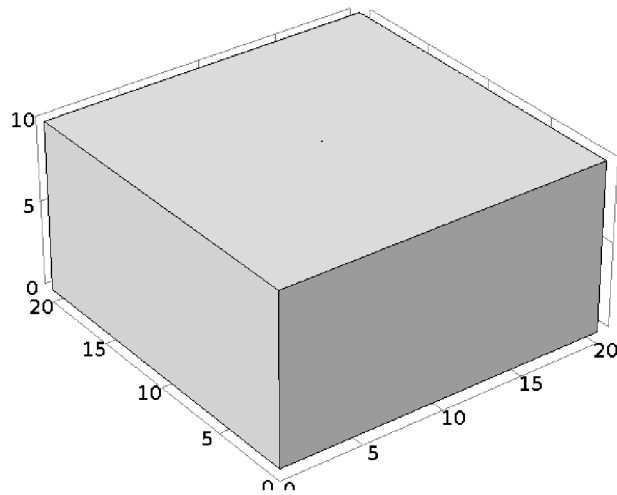
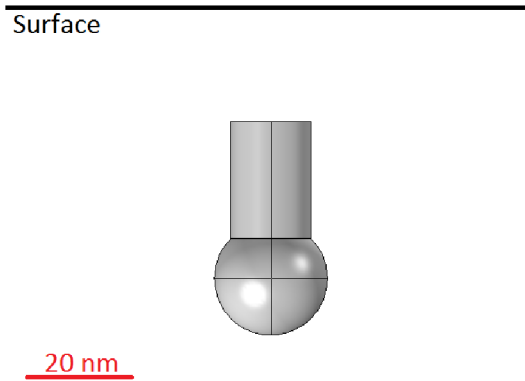Figure 3.7: Simulation block of Ge(100). Scale is in μm.

Figure 3.8: Geometry of the power source. The height of the upper cylinder is 43.4 nm and its radius is 15 nm, this cylinder contains 90% of the power. The radius of the lower sphere is 21 nm and this sphere contains 10% of the power. The upper edge of the power source is located 21.7 nm under the surface.

of the power. This setting of the power source is used so that it reflects the best the energy distribution shown in Figure 3.6.

From the results of simulation sample heating by current (shown in section 3.1.1), one can assume that the temperature field is uniform in a block of $20 \times 20 \times 10$ μm^3. This was used as a boundary condition, where all sides, except the surface side, of the simulation block were kept at constant temperature (500 °C in this case, but practically it can be set to any temperature in range 400-600°C if one assumes that thermal conductivity and heat capacity are not temperature dependant). The power source was set in the middle of the simulation block and 21.7 nm under the surface (in correspondence of energy distribution). The resulting temperature field is shown in Figure 3.9 and its cross-section is in Figure 3.10. The simulation was repeated for different powers, or rather a different electron beam currents.
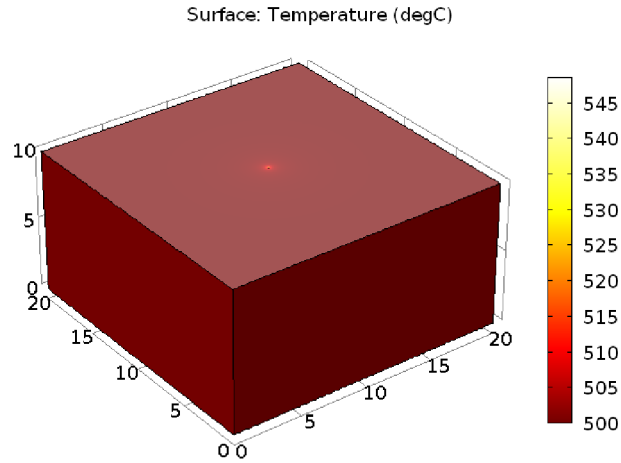
21

Figure 3.9: Overview of temperature field in the simulation block. The power source is in the middle of the simulation block. Electron beam current is in this case 25 nA. The dimension scale is in μm and temperature scale is in °C

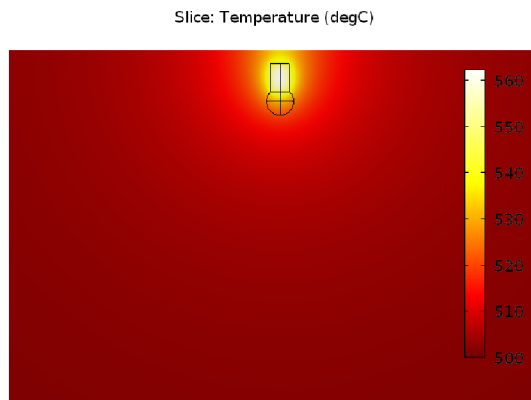
Figure 3.10: Cross section of the temperature field, with the power source in the middle. Temperature scale is in °C.

In order to highlight surface temperature field the data were exported from Comsol and were plotted Matlab. In Figure 3.11 is shown this temperature field with electron beam current 25 nA.

In Figure 3.12 are shown temperature fields for electron beam currents 5 nA, 25 nA, and 45 nA, also there are marked two borders of an example island with the diameter 400 nm and in the distance 400 nm from the power source. This reflects the typical situation when one moves the islands with the electron beam. The difference in temperature on one face of the island and on the other face is in units of °C and has a linear dependence on the electron beam current. Furthermore, these results show that the electron beam can indeed locally heat up the surface even by the tens of °C. This strongly supports the argument that an electron beam moves the islands by inducing a local temperature gradient.
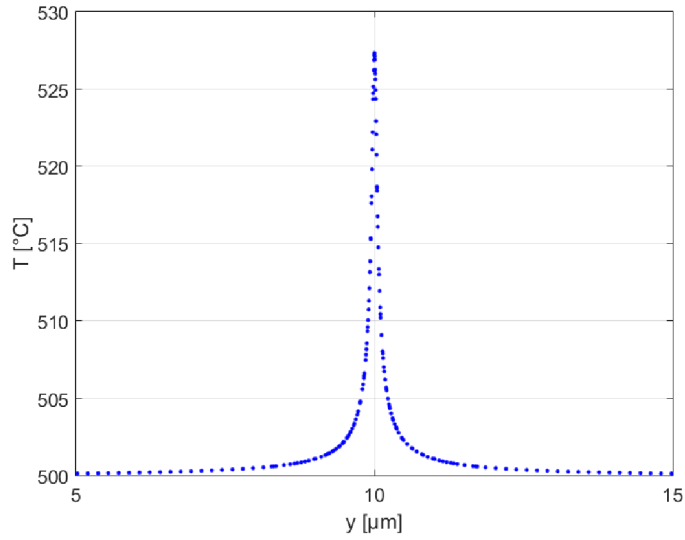
22

Figure 3.11: Simulated temperature field on the surface. Note that temperature field is rotationally symmetrical. Electron beam current is 25 nA.
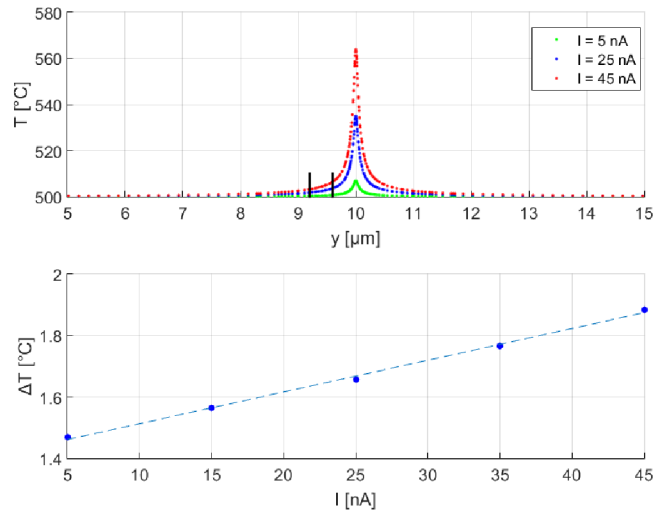

Figure 3.12: In the upper graph are shown different temperature fields with different electron beam currents used, namely 5, 25 and 45 nA. Two vertical black lines are marking the borders of a 400 nm AuGe island in 400 nm distance from the electron beam spot. Then in the lower graph is shown the temperature difference ΔT between the two borders of the island depending on the electron beam current. Note that this temperature difference has a linear dependence on the used current.

In addition, these temperature fields were also interpolated by linear interpolation. This was done in Matlab® with its curve fitting tool. One example of the interpolation is shown in Figure 3.13. Initially was the fitting tried by using analytical functions (exponential and gaussian). However it was not possible to reach the satisfactory
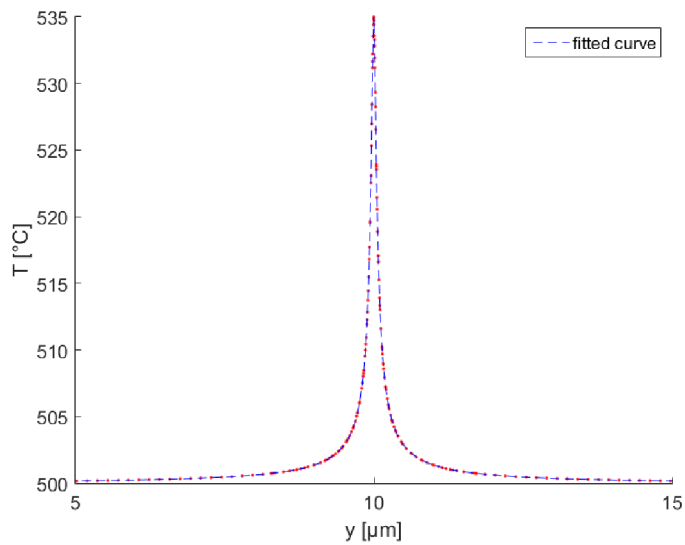
23

Figure 3.13: Interpolated temperature field. Linear interpolation was used. Used current is in this case 25 nA.

accuracy and thus the linear interpolation had to be used. In Figure 3.14 is shown an example, where the fitting was done by using an exponential function in form

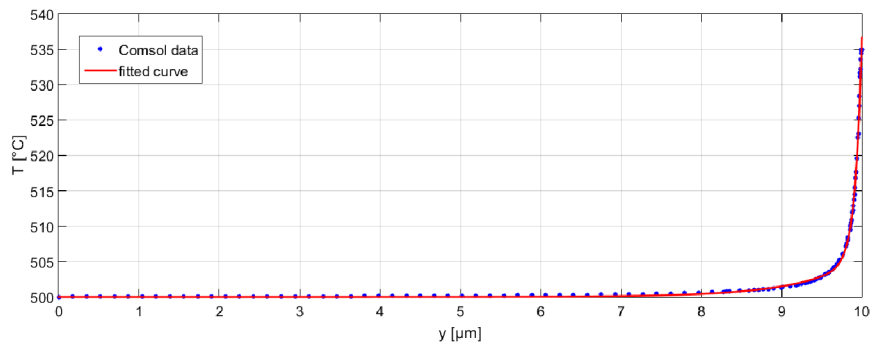$$T(y) = 500 + a \exp(by) + c \exp(dy).$$

Figure 3.14: Data from Comsol simulation fitted by the exponential function. The current used is 25 nA. Unfortunately this fit is too inaccurate to be used.

24

3.2 Experiments

3.2.1 Sample preparation and used instruments

As the substrate were used germanium wafers. Two types of crystallographic orientation substrates were used, namely Ge(100) and Ge(111). Samples were initially cut manually from the germanium wafer, however, due to the size randomness, were later samples cut by the laser cutter into $2 \times 10 \times 0.5$ mm^3 blocks (in the same fashion as the simulated sample in the section 3.1.1).

Gold nanoparticles of diameters 100 and 200 nm, were deposited on the samples via the gold colloidal solution. A small amount of solution was put on the germanium sample in the form of small droplets and then samples were heated in order to evaporate the solution. After the evaporation of the colloidal solution, there should be only gold nanoparticles remaining on the surface, however, as expected it is not possible to get rid of all the residual solution and there is always some left on the surface.

There was also an attempt to study the migration of islands on the graphene surface. In this case, two-layer graphene was put on the germanium substrate via electrolytic delamination. Then on this sample with the graphene were fabricated gold-germanium disks of different diameters via the electron beam lithography. These disks were used to create AuGe islands on the graphene layer. The whole process is shown in Figure 3.15. The lithography was more or less successful (see Figure 3.16), however, due to the very poor quality of the graphene layer and overall contamination, was this experiment dropped.
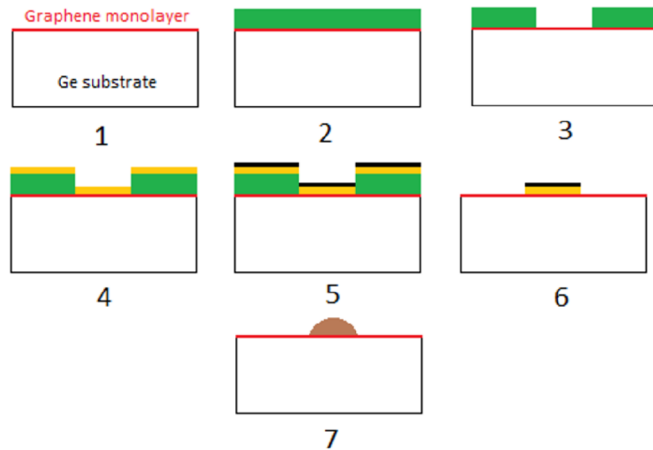

Figure 3.15: Schematic of fabricating process of gold-germanium disks. 1) initial sample, 2) application of PMMA resist (green layer) resist, 3) creation of patterns, 4) deposition of gold via the EBPVD (yellow layer), 5) deposition of germanium via the effusion cell (black layer), 6) lift-off, 7) annealing of the disk, which leads to AuGe island.
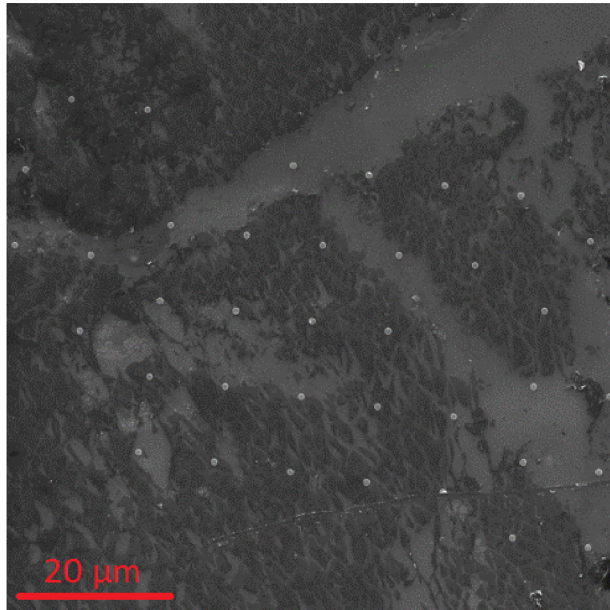
Figure 3.16: SEM image of the fabricated disks of diameter 900 nm. The darker part of the substrate is the graphene layer. Poor quality of the graphene layer is apparent.

Temperature gradient estimation experiment (section 3.2.3) was done on ultra high vaccum (UHV) scanning electron microscope (SEM) NanoSam (photo in Figure 3.17) by Scienta Omicron® company with built in hemispherical analyzer for Auger electron spectroscopy (AES). Reason why such specific SEM had to be used, is because it is capable of using electron beam currents above 10 nA. Such high electron beam currents were needed in order to induce the island migration. Later exper-
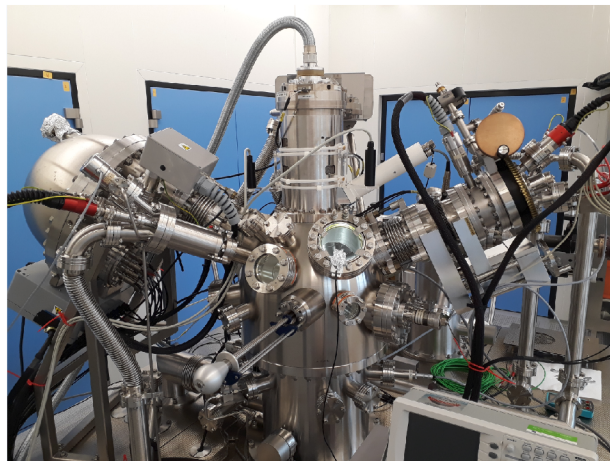

Figure 3.17: Photo of the UHV SEM Nanosam. This instrument was used in temperature gradient estimation experiment.

iments (fabrication of structures section 4.3) were done on experimental prototype UHV SEM (photo in Figure 3.18)made by Tescan® company. The reason, why experiments were switched to this instrument is that effusion cell, which was used for

26

germanium depositions, could be installed directly into the main chamber of SEM. This allows one to simultaneously use the SEM and run the deposition.
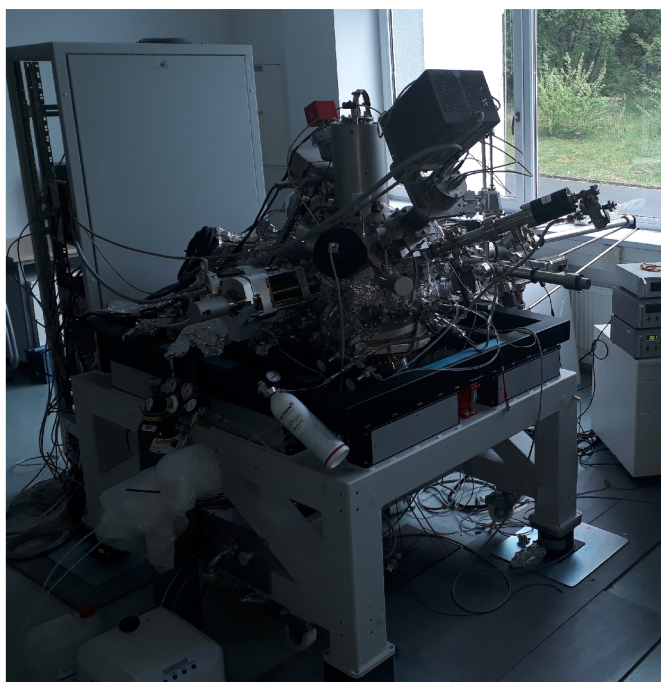

Figure 3.18: Photo of the Tescan UHV SEM. This instrument was used for fabrication experiments.

3.2.2 General observations in experiments

This section is a summary of islands behavior during the electron beam controlled migration, there are several observations, which occurred more or less during any experiment, where island migration was incorporated. These general observations are listed below.

- There is a critical size of an island and below the critical size, it is not possible to induce the island migration. This should not come as a surprise as it was already said in section 2.2.2. As previously stated, the existence of critical size is due to the increasing effect of interface kinetics as the size of the island decreases. In the observations, the usual limit was for islands around diameter 200 nm. Naturally, there may be also other effects that can influence this limit, for example, surface contamination plays a big deciding factor in this case, as in some cases it was relatively easy to induce migration of smaller islands (400-500 nm in diameter), while on some other samples it was impossible to move such islands. When islands were in the area with the residual colloidal solution it was much harder to induce the migration in comparison with the islands on a pure germanium substrate. In Figure 3.19 is shown an arrangement of smaller islands in the shape of the letter „A".
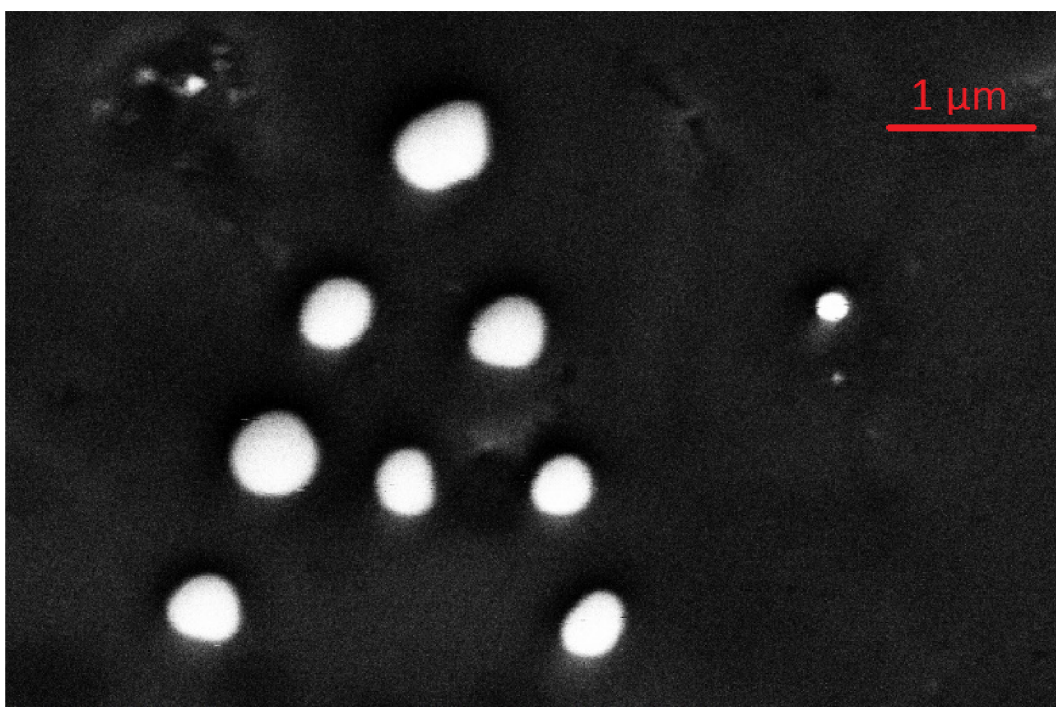

Figure 3.19: SEM image of arrangement of smaller islands in shape of letter „A". The smallest island has diameter 410 nm. Used substrate is Ge(111).

- The velocity of migration depends on used electron beam current (used currents were usually in range 10-30 nA). This is another property that should not

come as a surprise, as higher current means higher power, and thus higher temperature gradient (see Figure. 3.12 in the simulation section 3.1.3), which in correspondence with equations (2.14) or (2.11) means higher velocity. If electron beam current is too low (usually below 10 nA) no migration will be induced.

- While inducing migration by using a reduced scanning window in SEM (as shown in Figure 3.1), the velocity of migration depends on scanning speed. Another expected property arises. As the electron beam scans more slowly, it heats up the area more and thus the velocity of the migrating island is higher. For the fastest scanning regimes migration might not be even induced, as the area is not heated enough.

- Initially, when islands are forming from Au nanoparticles, their shape copies the surface crystallography, so on Ge(100) their shape is rectangular and on Ge(111) it is triangular. This holds true also for the dissolving face of the island. This is shown in Figure 3.20. It is easy to see three dissolving faces, thus one can also determine from this that substrate is Ge(111). Stationary islands retain then round „droplet like" shape.
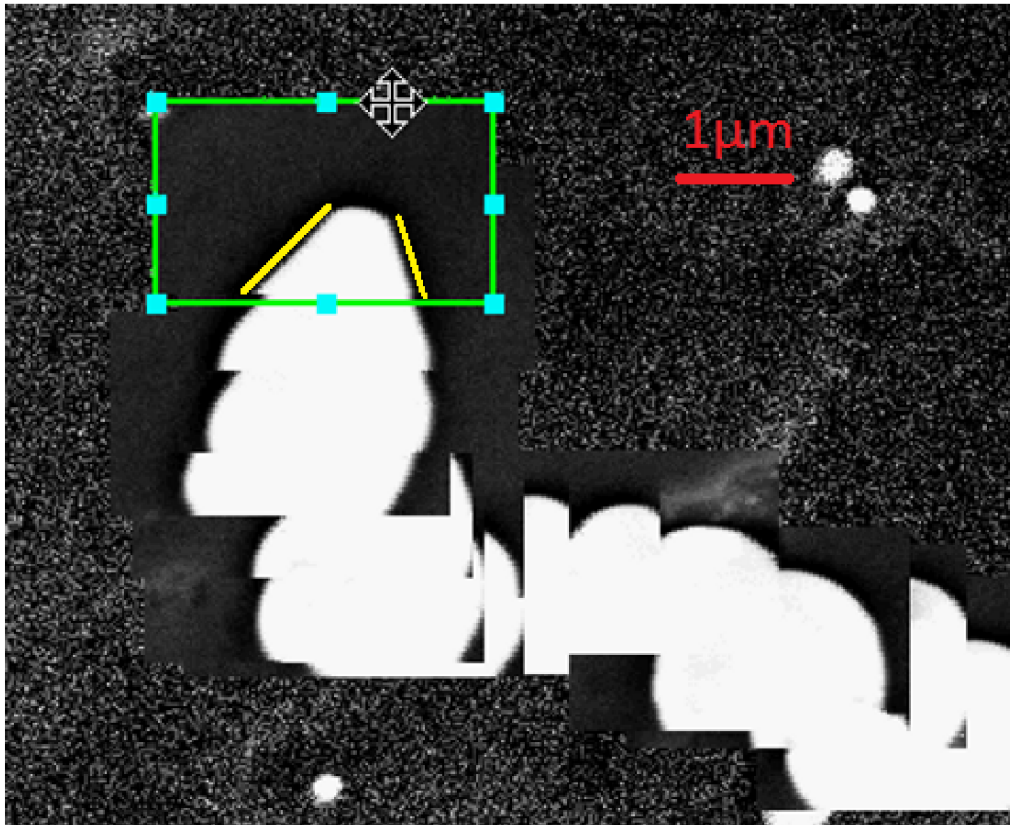

Figure 3.20: SE image of a migrating AuGe island. Two dissolving faces can be clearly seen in the figure and are highlighted by two yellow lines. The direction of migration is upwards. The substrate is Ge(111).

- As the island migrates it leaves behind itself a „groove", this is shown in Figure 3.21. Then the velocity of the island migrating back trough this groove is much higher. This is most likely because the island can dissolve the already deposited germanium much faster in comparison to when it has to dissolve previously untouched germanium. This means that interface kinetics have a smaller effect when the island moves through the germanium that was deposited during the initial migration.
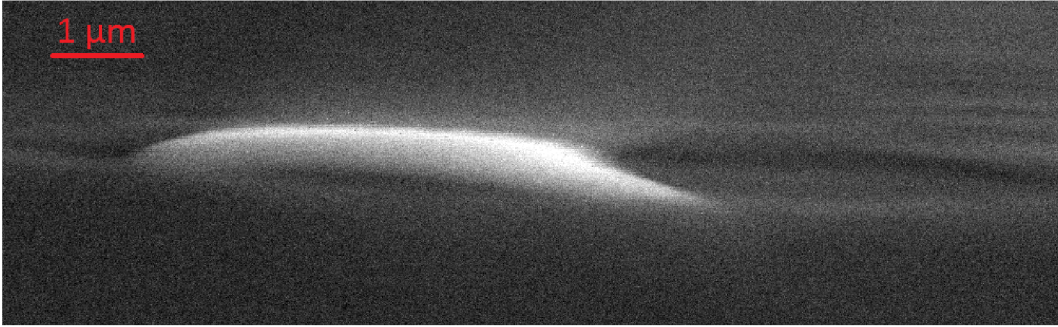

Figure 3.21: SEM image of a stationary AuGe island taken under a large angle. The island left behind itself a „groove" during migration.

- An operating temperature greatly influences the velocity of migration. It has been observed numerous times, that with the increasing temperature, the velocity of migration increases. Also increasing the temperature is the usual trick that one can use when it is impossible to move with an island at some temperature or velocity of migration is too low. The reason why the velocity increases is in the diffusion coefficient D in equation (2.14). The diffusion coefficient increases with the temperature, according to the Arrhenius equation, as

$$D = D_0 \exp\left(-\frac{\Delta H}{kT}\right).$$

Therefore, at a higher temperature, the higher velocity is to be expected. However, at the higher temperatures islands can evaporate, or if the migration is not induced they can „dig" too deep into the substrate.

3.2.3 Experiment for temperature gradient estimation

A simple experiment was designed to measure interaction distance between an AuGe island and the electron beam. Its result was then used in combination with results from the simulation of the temperature field induced by the electron beam.

Before starting the experiment, it was needed to measure the dependence of the current on the extraction voltage, as the current in the experiment was changed via change on the extraction voltage. This was measured via the Faraday cup and the result is shown in Figure 3.22.
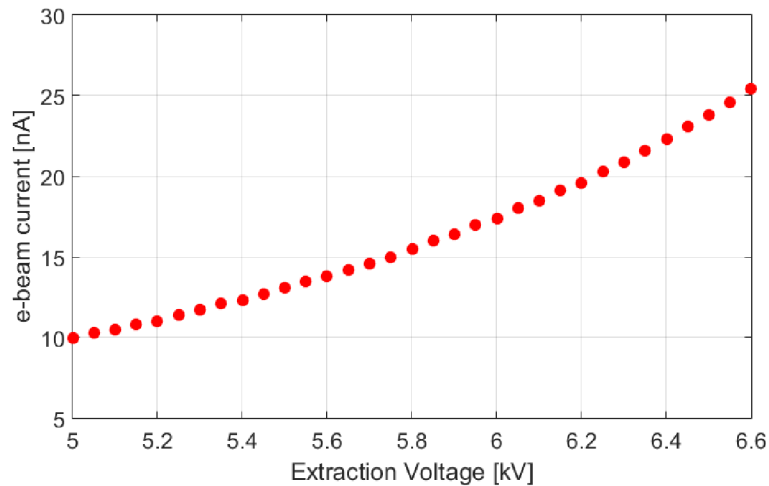
Figure 3.22: Dependence of electron beam current on the extraction voltage. Measured via the Faraday cup.

First, a groove was made with an AuGe island. This groove was then used as a „track" for measurement of the interaction distance. This was necessary because velocities in the groove are more stable and this allows one to repeat the measurements.

The procedure of the experiment is described as follows. Point scanning was used, so an electron beam is placed only on one spot at the time. The beam was put in a 2 μm distance from the edge of the island. Then it was brought closer to the edge of the island. At this point full SEM image (fast scan) was taken to see, whether the islands moved towards the targeted spot. This was repeated until the island moved, at this occurrence, the distance of the target from the edge has been recorded (shown in Figure 3.23). Then the electron beam was increased and the whole procedure was
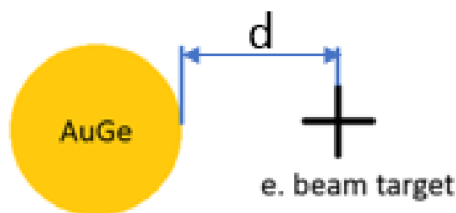

Figure 3.23: Schematic of the experiment. The island was approached by the electron beam until it observably moved, then the distance d was recorded.

repeated. The whole experiment was done for the island of diameter 400 nm and for the island of diameter 700 nm. Results are in Figure 3.24. There can be clearly seen a linear trend for both islands. This nicely relates to the linear trend in Figure 3.12 (section 3.1.3), where the temperature difference between the front and rear faces of a hypothetical island is also linearly dependent on the electron beam current. Fitted

31

functions were in following form

$$d(I) = aI + b. \tag{3.2}$$

Coefficients a, b and coefficients of determination (R^2) are shown in Table 3.1. It is

	a	b	R^2
400 nm	24.11	72.68	0.9965
700 nm	23.39	157.5	0.9957

Table 3.1: List of coefficients for fitted linear function shown in equation (3.2).
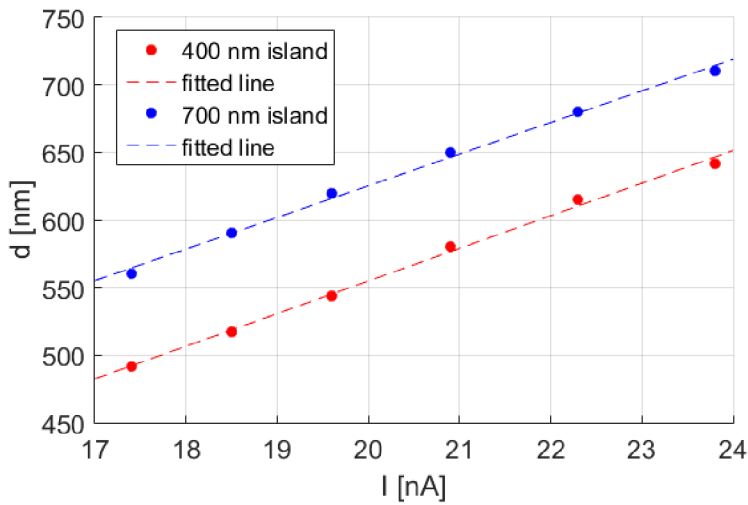

Figure 3.24: Distances between the edge of an island and target of the electron beam, at which island moved. A linear trends can be seen from fitted functions.

clear that coefficient b is dependent on the size of the island, which is to be expected as the temperature gradient will have stronger influence on the larger islands and thus larger island will be able to move at larger distances from the electron beam. Meanwhile coefficient a is nearly identical for both island sizes. This indicates that the size of the island has a weaker influence on the slope of the line. This will be also be discussed below in Figure 3.29.

3.3 Combination of simulation and experiment

When both simulation (section 3.1.3) and experiment (section 3.2.3) were done, their combination was used to roughly estimate the temperature gradient (or rather temperature difference between the front and rear face of an island) that was needed to start the migration of islands described in the experiment section. To simply estimate this temperature difference, distances recorded in the experiment were put into simulated temperature fields, and the temperature difference between the front

and the rear face of the island was recorded. Naturally, used temperature fields were simulated for the currents used in the experiment. Graphs of these temperature differences are shown in Figures 3.25 and 3.26. Also the mean temperature difference was calculated, for 400 nm island $\overline{\Delta T} = 0.89 \pm 0.04$ °C and for 700 nm island $\overline{\Delta T} = 1.00 \pm 0.02$ °C.

The result of this combination of experiment and simulation is that the temperature gradient needed to induce the migration does not depend on the electron beam current. On the other hand, it does depend on the size of the island. These results are in agreement with predicted models.
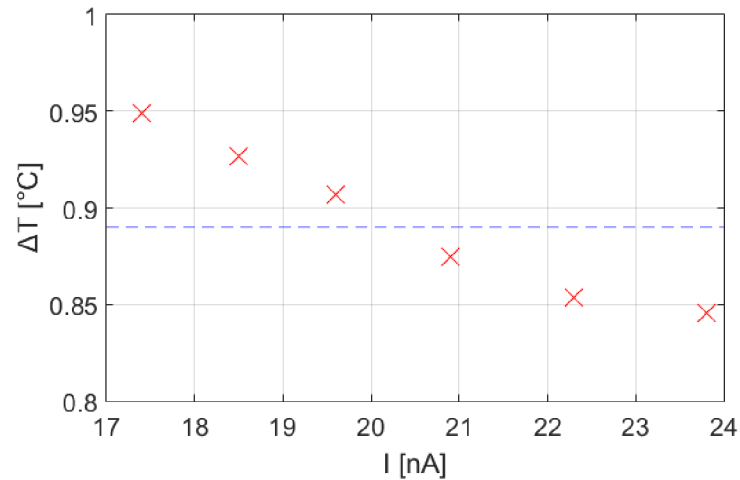

Figure 3.25: Temperature differences between the front and rear faces of the 400 nm island. Blue dashed line marks the mean value ($\overline{\Delta T} = 0.89 \pm 0.04$ °C).
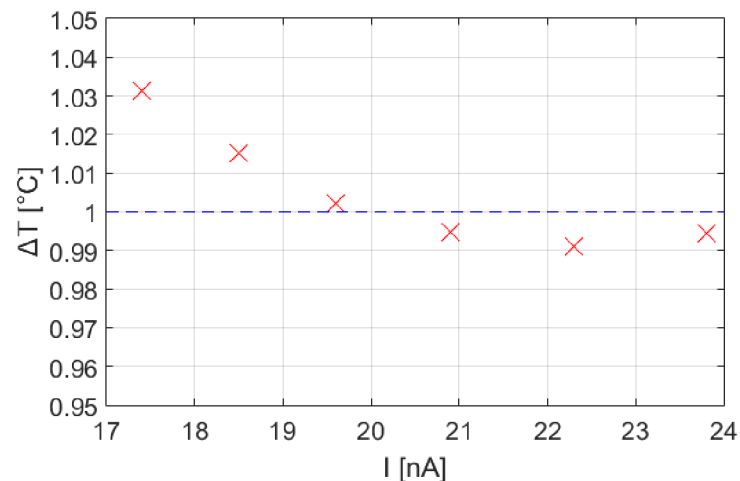

Figure 3.26: Temperature differences between the front and rear faces of the 700 nm island. Blue dashed line marks the mean value ($\overline{\Delta T} = 1.00 \pm 0.02$ °C).

In the following step were used the interpolated data (see Figure 3.13) and the estimated temperature differences (above). By using these known temperature differences and functions it is possible to retrospectively determine the distances at which the known temperature difference occurs. Then it is possible to compare these distances with the distances from the experiment (see Figure 3.24). These comparisons are shown in Figures 3.27 and 3.28. It is clear that, for both 400 nm and 700 nm island are results quite good as the fitted lines between the points are very similar. The 700 nm island result is slightly better as the slopes of both lines are nearly identical.
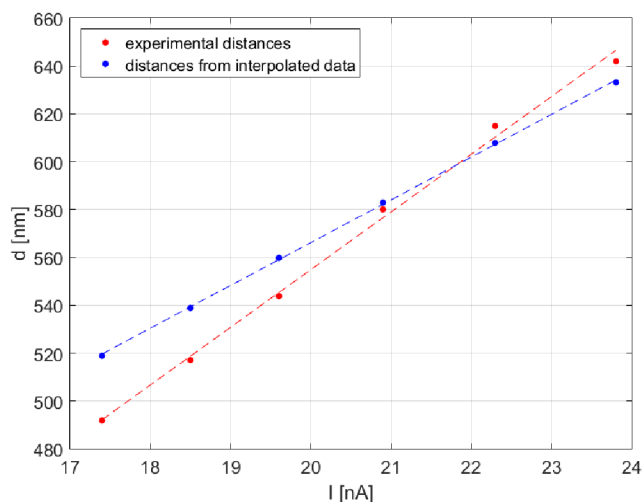

Figure 3.27: Comparison between the distances determined from the fitted functions and the experimental distances at which the 400 nm island moved.
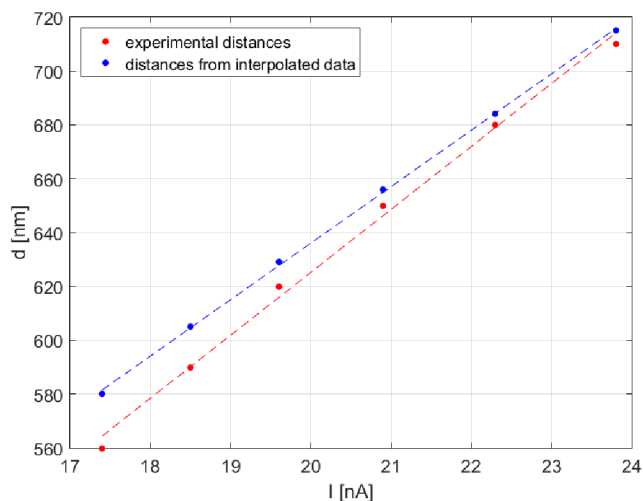

Figure 3.28: Comparison between the distances determined from the fitted functions and the experimental distances at which the 700 nm island moved.

Lastly, a variation of parameters was done to see the influence of the temperature difference and size of the island. Variations is shown in Figure 3.29. The idea was to vary the needed temperature difference (values of dT = 0.5/1/1.5 °C were used) and for each selected temperature difference the size of the island was varied (values of 500/600/700/800/900 nm were used).

It is clear that if one considers a fixed temperature difference for each size it has a significant influence on the slope and also the position. However, as it has been shown in Figures 3.27 and 3.28 each size has a different temperature difference, which is needed to induce the movement. From this unclear relationship between the size and temperature difference arise difficulties when one tries to interpret the influence of both parameters. Moreover, one has to keep in mind the error of the simulation and experiment and assumptions that had to be made (mainly the 80% energy to heat conversion, see Section 3.1.3).
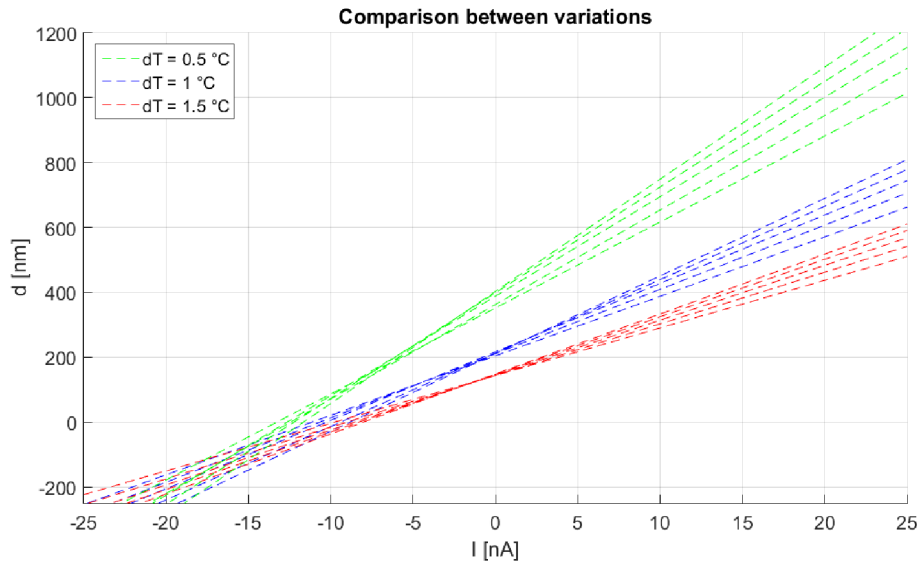

Figure 3.29: Comparison between variations of temperature gradient (which is needed for island to move) and island sizes (the steepest slope is always for the largest size, while the flattest slope is for the smallest size of an island).

Chapter 4

Fabrication of structures by utilizing the island migration

This part of the thesis describes the first potential practical application of the electron beam induced AuGe island migration, which is the fabrication of structures by using the combination island migration and the vapor-liquid-solid (VLS) growth method.

The liquid eutectic islands became quite popular in the nanosciences when Wagner et al. [34] utilized AuSi liquid islands for the growth of nanowires and named it as the already mentioned VLS method.

As the growth of nanowires is a crucial part of this thesis, a brief preview of nanowires (namely the fabrication techniques) is presented in the section below, before the actual description of the proposed practical application (section 4.2). Then the experiments and results are presented (section 4.3).

4.1 Nanowires

Nanowires (nanowhiskers, NWs) are structures with the diameter of the order of nanometers. Typical length-to-width (aspect ratio) of NWs is 1000 or more and they are often referred to as 1-D materials. Therefore, NWs can exhibit quantum confinement effects as electrons in NWs are confined laterally. This confinement in lateral direction leads to energy levels that vary from the usual continuum energy levels or bands found in the bulk material.

For example, certain NWs have discrete values of electrical conductance which are often referred to as the quantum of the conductance and are integer multiplies of $2e^2/h$ (where e is the electron charge and h is Planck's constant) [35].

Additionally, their one-dimensional geometry on the nanometer scale provides a very high surface area with a nanoscale radius of curvature and great mechanical flexibility [36].

These interesting properties of NWs make them very attractive for various science and engineering disciplines such as nanoelectronics, biology, and more. For instance, in 2012 M. Mongillo et al. [37] were able to create a NAND gate (see Fig. 4.1) from

undoped silicon NWs. This avoids the problem of precision doping of complementary nanocircuits.
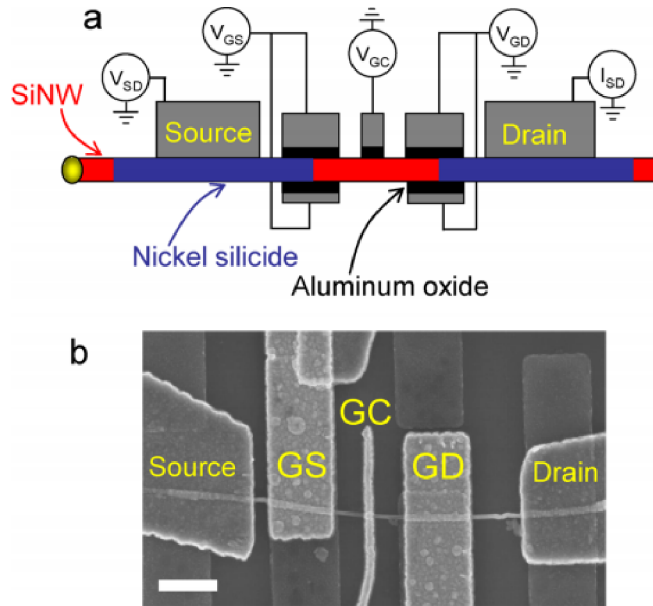

Figure 4.1: (a) Schematic of NAND gate created from a single undoped Si NW. Wrap gates labeled as GS and GD control the Schottky barriers at the silicon-silicon junctions formed by the source and drain contacts. The finger gate in the middle GC controls the carrier population in the silicon channel. (b) SEM image of the device. The scale bar is 400 nm. Taken from [37].

The size of these materials is also comparable to visible light in the wavelength range from 400 to 650 nm which means that NWs can also be used for advanced optoelectronics [36] (e.g. Nanowire lasers [38]).

4.1.1 Top-down technique for NW fabrication

As the name suggests a top-down approach reduces a large piece of material to small pieces. This can be achieved by various approaches. The most known top-down technique would be the *lithography*, where a layer of a sensitive material (called resist) is applied on the surface. Then a pattern is carved into the resist using either a light (photolithography) trough the prefabricated photomask or an electron beam (Electron beam lithography) in which the electron beam is directly „drawing" the pattern into the resist. After the pattern is finished, a material is deposited on the surface. Then the sample is chemically etched, leaving the deposited material only in areas selected by the carved pattern.

As an example serves [39], where $Al_2O_3/ZnO/Al_2O_3$ coaxial nanotubes were made by utilizing several fabrication methods, such as deep-UV lithography, atomic layer deposition (ALD) and plasma etch methods. The whole fabrication process is shown in the Figure 4.2.
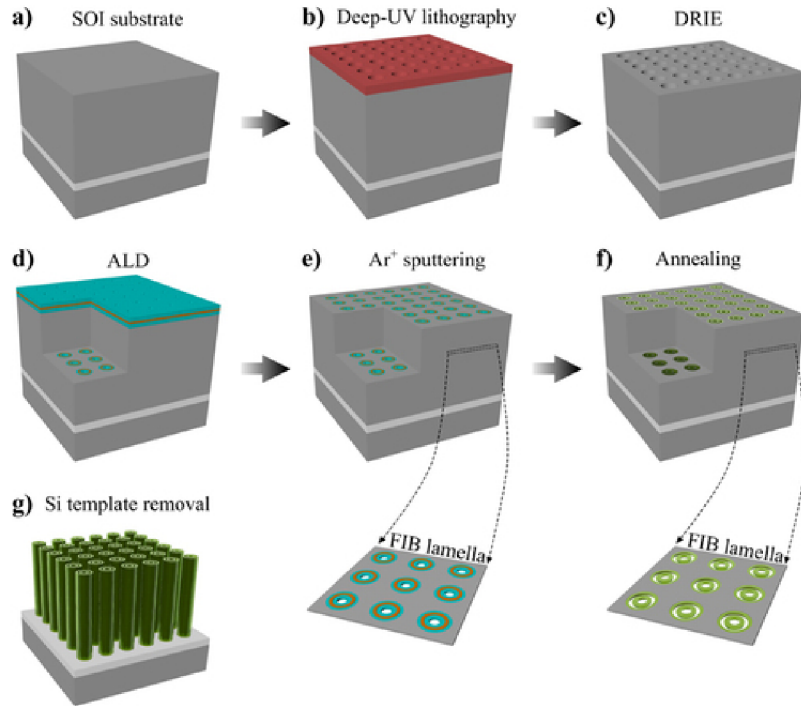
Figure 4.2: Fabrication process of nanotubes. (a) silicon-on-insulator wafer (SOI). (b) Deep-UV litography. (c) Template prepared by DRIE. (d) Deposition of materials using ALD. (e) Sputtering of ALD deposited cap layers. (f) Annealing at 800 °C. (g) Isolation of tubes by etching of the silicon template. Taken from [39].

There are also other top-down methods such as milling and thermal oxidation but as top-down techniques are not important for this thesis they are not discussed in detail.

4.1.2   Bottom-up techniques - VLS

More popular approaches for NWs synthesis are bottom-up techniques. There are various bottom-up techniques, but for NW synthesis one is particularly important and is utilized in this thesis, namely the *Vapor-Liquid-Solid* (VLS) method.

The VLS mechanism was originally given by Wagner and Ellis [34] in 1964 as an explanation for the unidirectional growth of Si whiskers (wires) [40]. The explanation was motivated by the i) absence of screw dislocations in the whisker, ii) the presence of impurity is necessary, iii) small droplet is present at the tip of the growing whisker. Ever since then the VLS has grown in popularity and was confirmed numerous times [41][42].

The VLS mechanism   is a 1D crystal growth mechanism that is assisted by a metal catalyst. Figure 4.3 shows a simple schematic of the VLS mechanism. The first step is to supply the metal catalyst onto the substrate. The most common way of supplying the metal catalyst is to deposit a thin metal film (Fig. 4.3a) on the

surface by sputter deposition or thermal evaporation. In this work, another approach is used (see section 3.2.1). Then the sample is heated and the deposition of precursor elements begins (Fig. 4.3b). At a temperature higher than the eutectic point (see Figure 4.4), the metal absorbs components from the vapor and/or substrate and forms liquid alloy islands. For some reason (temperature, vapor pressure fluctuation) the alloy becomes supersaturated. That means that it becomes a solution with the higher actual composition of the components than the equilibrium concentration. As the droplet becomes more and more supersaturated, it starts to precipitate its components at the liquid-solid interface in order to minimize the free energy of the alloy system. Subsequently, the 1D crystal growth begins (Fig. 4.3d) and it continues as long as the vapor components are being supplied or till the metal catalyst completely evaporates from the tip of freshly grown NW. As all of the phases are present: the vapor (carries solid components), liquid (catalyst alloy), solid (grown NWs), hence the name VLS mechanism [36].
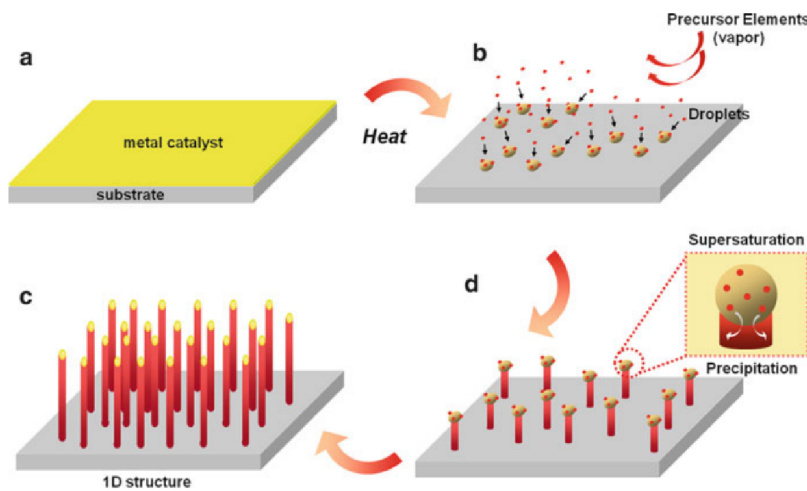

Figure 4.3: Growth of the NWs by VLS mechanism. Taken from [36].

Metal catalyst is essential in the VLS mechanism, however not all metals will work. Several requirements must be fulfilled in order for metal to qualify as a suitable catalyst for the VLS:

- It must form a liquid solution with a solid phase component.

- The solubility limit of the metal in the liquid phase must be higher the solubility limit in the solid phase (i.e. $K = C_s/C_l < 1$, where $C_{s/l}$ is the solubility limit in solid/liquid phase). With this condition fulfilled, the catalyst should easily form the liquid alloy with little contamination in the solid phase.

- The vapor pressure (V_p) of the metal in the liquid alloy should be small. Otherwise, the metal will evaporate from the liquid alloy before the NW will be grown.

- It must be inert to chemical reactions, as the reactions could deprive it of its catalytic function.

- It must not form an intermediate solid which would also deprive it of its catalytic function.

Generally, noble and transition metals usually work well with the VLS mechanism. The most popular metal used is gold, which is also used in this thesis. It works well for the growth of NWs of group IV materials (Si, Ge), oxides (ZnO), and also III-V semiconductors [36].

A phase diagram is very useful as the adsorption, dissolving, mixing, diffusion, and precipitation in the liquid phase are thermodynamic processes that aim toward an equilibrium. Therefore, the phase diagram can be used to predict catalyst functionality. As an example serves the Au-Si system (Fig. 4.4). From the diagram, it can be clearly seen that the minimum growth temperature has to be higher than the temperature of the eutectic point of the system (363 °C). Additionally, the composi-
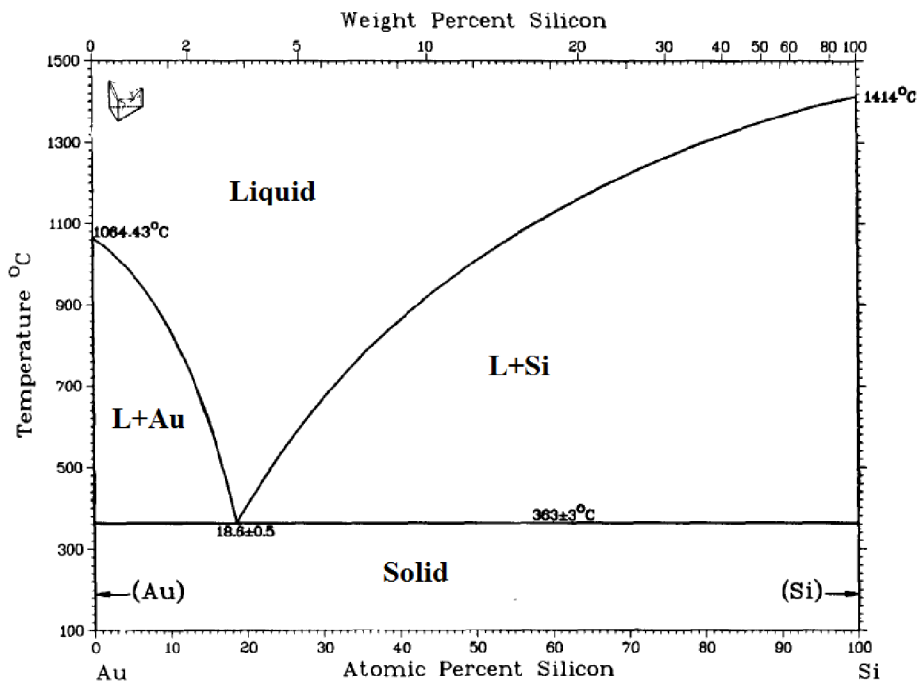

Figure 4.4: Phase diagram of Au-Si system. Taken from [14]

tion of the Au-Si alloy will follow the liquidus line, which determines the equilibrium between the solid and the liquid phase. However, temperature or vapor pressure fluctuation over the liquid alloy causes it to dissolve more Si than the equilibrium composition, and consequently, the alloy will be in a supersaturated state. In the phase diagram, this means that composition shifted to the right of the liquidus line. As the supersaturation state is thermodynamically a nonequilibrium state, it drives

the precipitation of the solid phase at the solid-liquid interface from the supersaturated liquid alloy, until the equilibrium composition is reached (composition shifts back to the liquidus line). This process repeats causing additional growth.

Additionally, it should be noted that available phase diagrams (such as Fig. 4.4) are measured from the bulk systems. However, the thermodynamic properties of a nanosystem can significantly differ from that of the bulk system. Therefore also phase diagram of the nanometal catalyst should differ and it is indeed the case. For example in [43] the equilibrium composition of nanoscale AuGe alloy droplets at the tips of Ge NWs has been investigated and it has been found that it significantly deviates from that of the bulk alloy (see Fig. 4.5). This can lead to discrepancies between the actual growth behavior of the NWs and predictions based on the phase diagrams of the bulk systems [36].
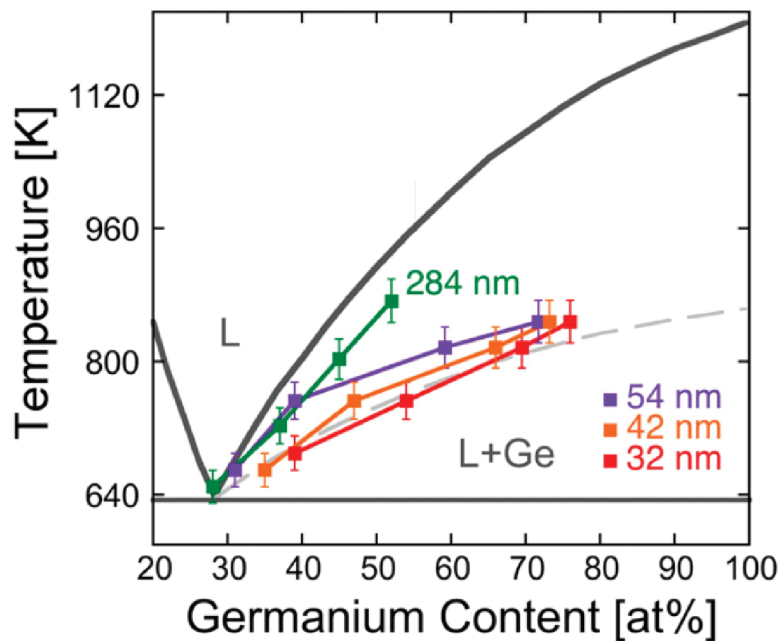

Figure 4.5: AuGe phase diagram. The gray lines represent liquidus and solidus lines. Squares represent measurements of the temperature-dependent Ge content of AuGe alloy droplet at the tip of the Ge NW. Taken from [43].

4.2   Proposed fabrication method

Finally, the proposed method for the controlled fabrication of nanostructures is described in this section. Since one can use liquid AuGe islands for the growth of nanowires, and as we are able to move with these islands via the electron beam induced migration, a combination of these two mechanisms could yield an entirely new fabrication method.

The idea is to deposit germanium to the substrate, then at the right conditions, the VLS growth will be initiated. When the VLS growth is initiated one can move the island via the electron beam induced migration. The island trajectory can be an arbitrary pattern. As the island moves, it should also leave a new layer of material behind it because the VLS growth is also taking place. After finishing the complete pattern, the first layer is completed. Then the island can start moving again through the pattern, effectively leaving behind itself a second layer of the deposited material. In principle, this method should work similarly to macroscopic 3-D printing. Whole process is summarized in Figure 4.6.

Naturally, this is how the method should work in an ideal case. In reality, the island always dissolves some material from the substrate and subsequently deposits it back. There is no guarantee that the island will be depositing dissolved germanium in such a nice controlled way as shown in Figure 4.6.

Lastly, what could also happen is that it would be impossible to induce the migration of the island, while the VLS growth is running, as both processes involve dissolution and subsequent deposition of material. Fortunately, this was not such a case, as in experiments it was possible to move islands, while the deposition of germanium was running.
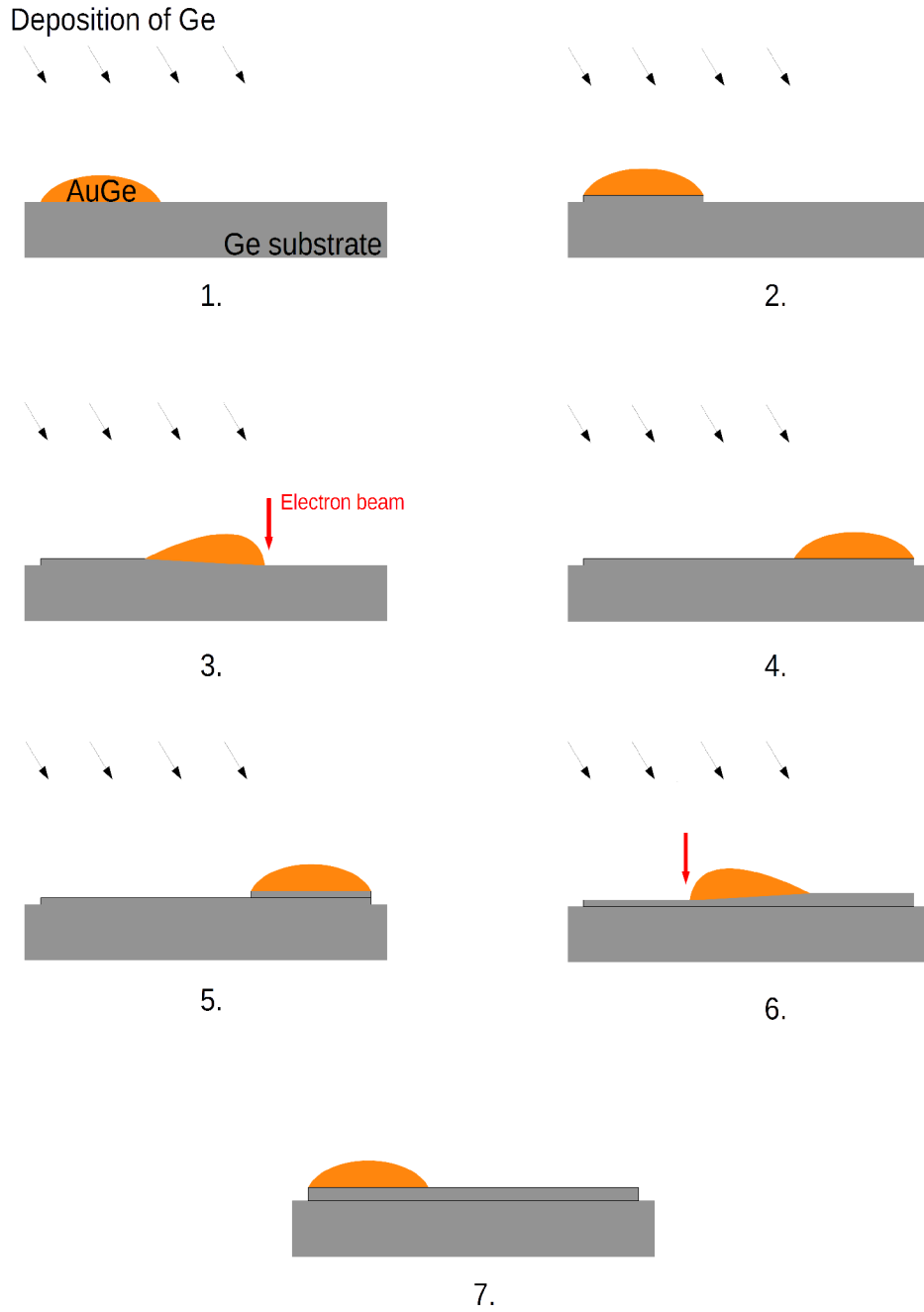
Figure 4.6: Schematics of nanostructure fabrication via the combination of VLS growth and electron beam induced island migration. In this case, the pattern is a simple line. 1) Start of the deposition of the germanium. 2) A layer of material is deposited under the island via the VLS growth. 3) Island is being moved by electron beam, while simultaneously depositing material under itself. 4) At the end of the line first deposited layer is completed. 5) The second layer of material is being deposited. 6) The island is being moved to the other end of the line, while still depositing the second layer. 7) After turning the deposition off, the VLS growth is turned off and the result is a two-layer line.

4.3 Experiments

This section deals with experimental work done on the proposed fabrication method. This includes preparations for the fabrication method such as growing the nanowires and trying to induce the migration of islands during the germanium deposition. These preparations were needed before actually trying the proposed method.

Simultaneous use of SEM and effusion cell

A germanium effusion cell was installed directly into the main chamber of the Tescan UHV SEM. Functionality, of both instruments running simultaneously, was tested. Fortunately, it was possible to run the deposition and the SEM without any complications.

Then it was checked, whether it is possible to induce the island migration when the deposition was running. This also proved to be possible. In Figure 4.7 is shown a detail of AuGe island, which was moved through the freshly deposited germanium. Deposited germanium can be seen in an SEM image as bright small islands. It is clear, that AuGe island dissolves freshly deposited germanium. In Figure 4.8 is shown an SEM image of islands trajectory through the freshly deposited germanium. This can be seen as a change in SEM image contrast because the germanium substrate remains dark, and thus islands trajectory is clearly visible.
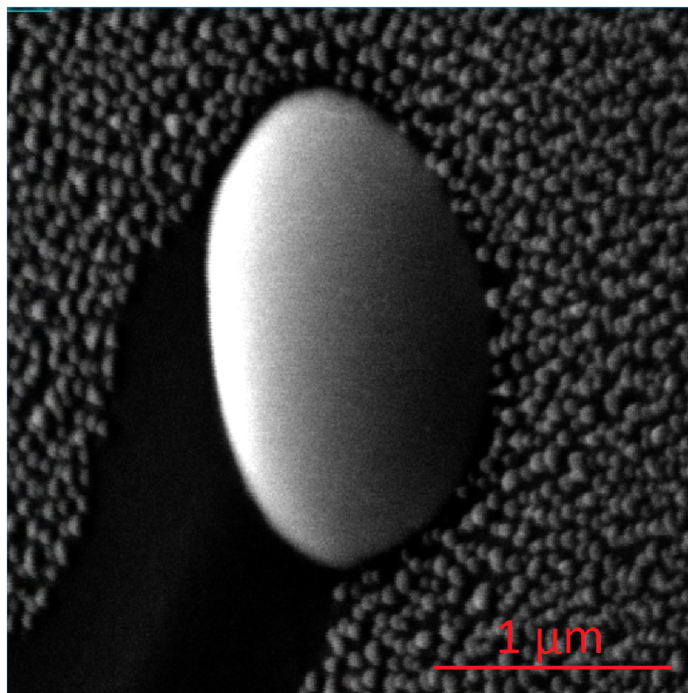

Figure 4.7: SEM image of AuGe island near the freshly deposited germanium. Deposited germanium appears as bright small islands in the SEM image, while the germanium substrate remains dark.
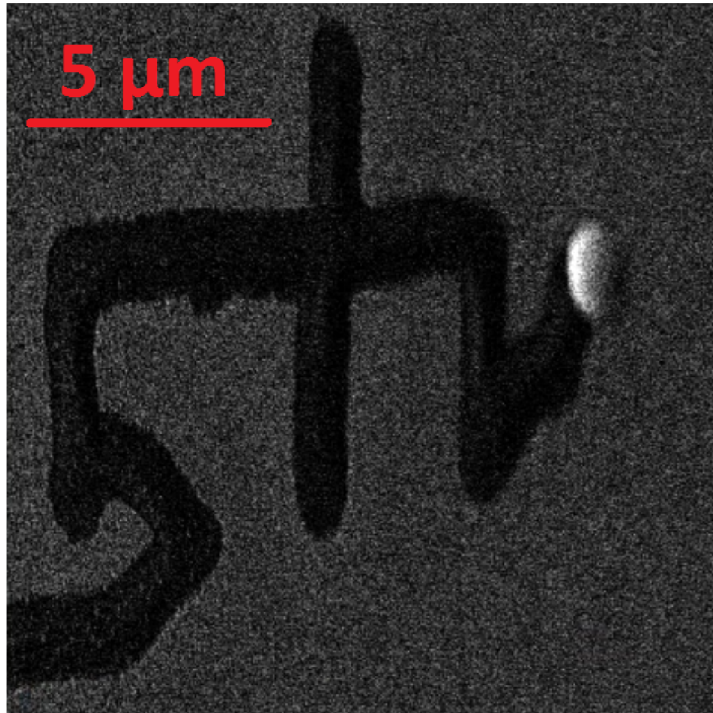
Figure 4.8: Overview of islands trajectory trough the deposited germanium. The trajectory is shaped as „5tv".

Additionally, **Stanli Hakira** developed software for the automatic movement of the electron beam. This software was developed for the automation of our proposed fabrication method, as it would be very tiring if the user had to move the AuGe island manually during the deposition time. This automation also allows more precise control of the trajectory of the island during the deposition, which means more precise fabrication patterns. Currently, the software can only move the island back and forth in a straight line. However, this line movement is currently sufficient enough for fabrication method testing. Later, the software can be extended to move the island in a more complex manner.

Overview of the software functionality is demonstrated in Figure 4.9 and works as follows. Users can select a starting point of the line and then select the ending point of the line. When the process is started, the software always scans in the reduced scanning window around the island in order to induce its migration, then it makes full SEM image to show the user that island moved and then again moves the reduced scanning area in a selected line to move the island to the next point of the line and again makes full SEM image. This cycle continues until the reduced scanning window reaches the end of the selected line and at this point, it goes back. This effectively moves the island back and forth through the selected line. Moreover, Stanli also implemented into the software function that allows users to change a scanning speed of the reduced scanning window and also the scanning speed of the full SEM image.
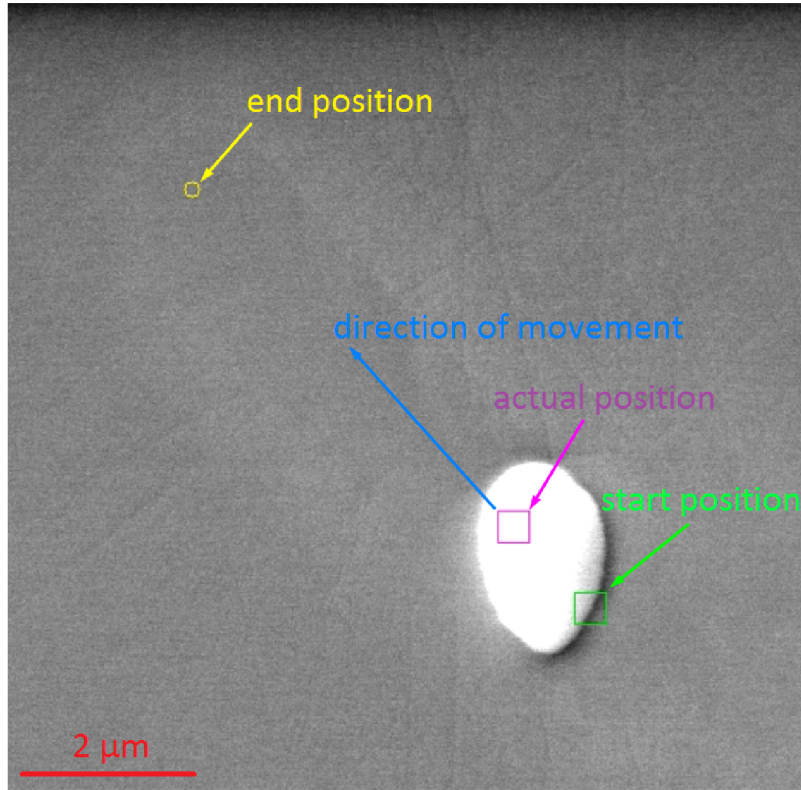
Figure 4.9: Image of the Stanli Hakiras software for automatic movement of the electron beam. Reduced scanning window (purple square) cycles between the starting and ending positions, while also dragging the AuGe island with it.

4.3.1 Growth of the nanowires

Naturally, if the proposed fabrication method is to be successful, it had to be checked, whether it is possible to even induce the VLS growth in our instrument setup. This has been tried several times as the VLS growth is no simple method and requires precise control of sample temperature and also precise control of sample position and angle to the effusion cell. This is because, according to users experienced in nanowires growth via the PVD deposition method (effusion cell), nanowires will grow only at some temperatures, which had to be determined experimentally, as in our instrument setup we had no way of directly measuring the sample temperature. With the temperature measurement out of the question, we had to simply try different heating currents until the growth of the nanowires was observed.

Successful nanowire growth was observed at the temperature close to the eutectic point (expected temperature around 400 °C) of the AuGe system (361 °C). This temperature was selected at the heating current ($I_{heat} = 0.5$ A), where AuGe island was becoming immobile (velocity of electron beam induced migration was very low). At this temperature, the deposition of germanium was started. After roughly an hour of deposition growth of nanowires was clearly observable. Then SEM images were taken 20 and 40 minutes after the first observation. The growing process is shown in

Figure 4.10. Detailed image of grown nanowires after the deposition was stopped is shown in Figure 4.11.
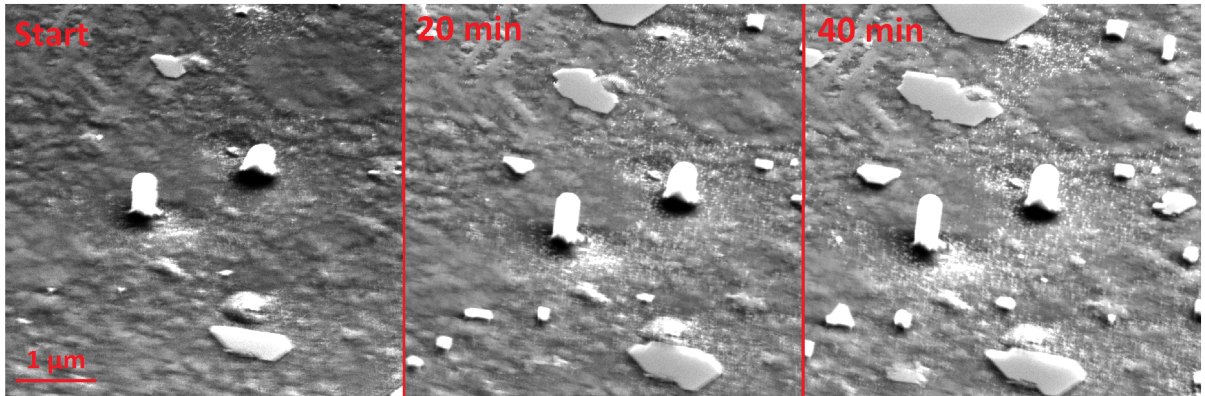

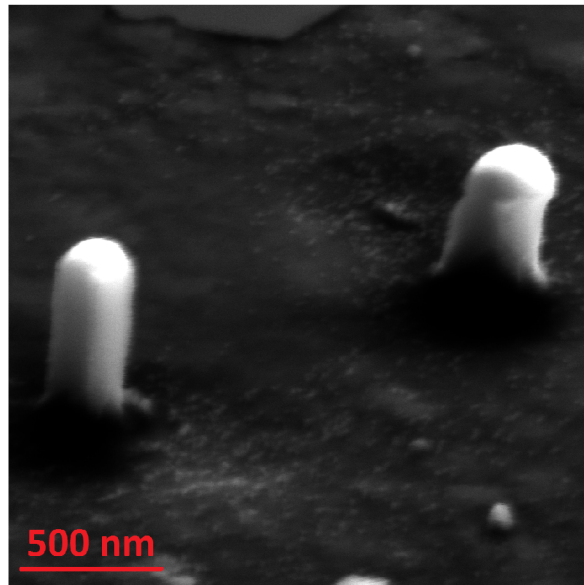Figure 4.10: Time sequence of growing nanowires.

Figure 4.11: Detailed SEM image of grown nanowires after the deposition was stopped. AuGe droplets can be clearly seen at the tips of NWs.

4.3.2 Experimental fabrication method

With everything tested and working it was time to try our new proposed fabrication method of nanostructures. It has taken quite some time and many tries and fails until the first observable result was yielded. However, in the end, I was able to grow a structure by combining the growth of the nanowires with the electron beam induced AuGe island migration. A grown structure, as it will be shown, is not perfect as it is the first observable result, nevertheless, it proves that the method is working if everything is set properly.

Now let's describe the procedure that has been taken before showing actual results. First, the sample was positioned against the effusion cell in a way that nanowire growth was observed at this position on previous samples. Then the sample temperature was elevated with the heating current $I_{heat} = 0.5$ A. Then a mobile AuGe island was found on the sample. At this point, the deposition of germanium was started. Flux current of the effusion cell was around 65 nA. When the bright deposited germanium islands started appearing, the Stanli Hakiras software was started. The AuGe island was being moved back and forth in a line by the automated electron beam. After roughly an hour of deposition, the bright structure started appearing at the trajectory of the island. The process was continued for another two hours and then software was stopped. Island was removed from the area, where it was being moved. A sequence of SEM images taken during the individual steps is shown in Figure 4.12. Resulting structure is shown in Figure 4.13.
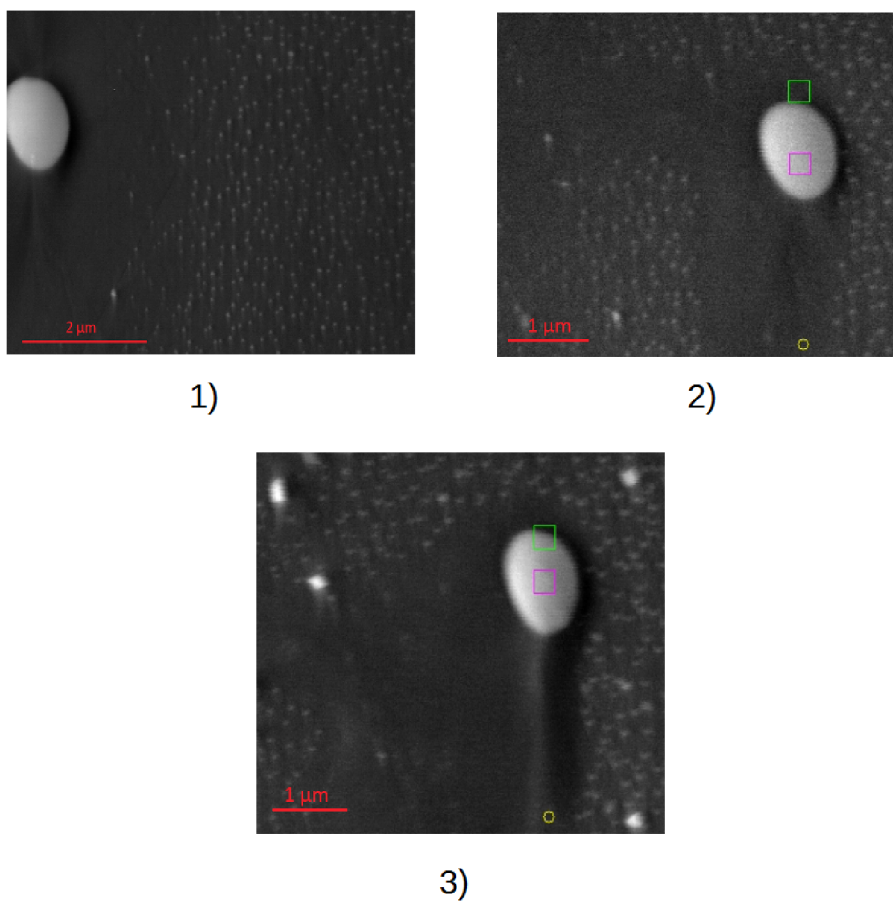

Figure 4.12: SEM images taken during the procedure. 1) AuGe island was moved to the area where germanium islands were nucleating. 2) Start of the software for automatic electron beam movement. 3) After a roughly hour a bright structure can be seen at the trajectory of the island.
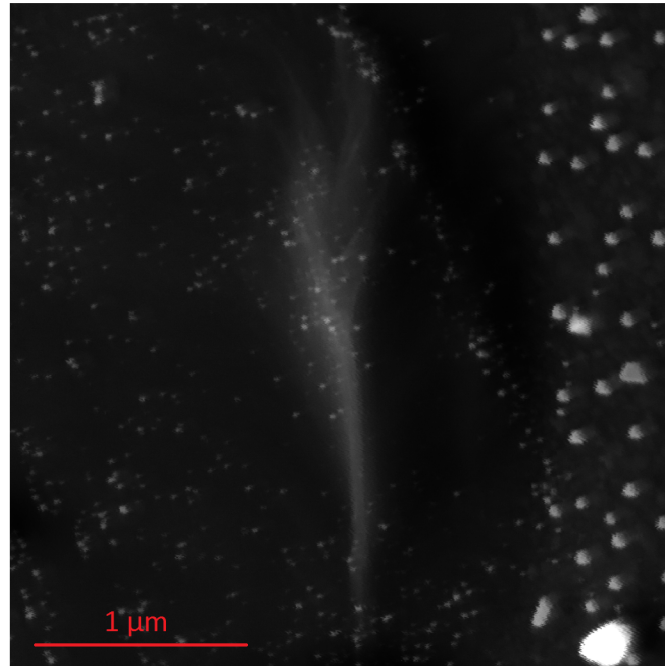
Figure 4.13: Resulting structure after roughly 3 hours of combined island movement and deposition of germanium.

Additionally, **Radek Dao** has made an AFM image of this structure. AFM image is shown in Figure 4.14. From the results of AFM measurement, the height of the grown structure is around 100 nm (see Figure 4.15) and it is shaped as a „broad mountain".
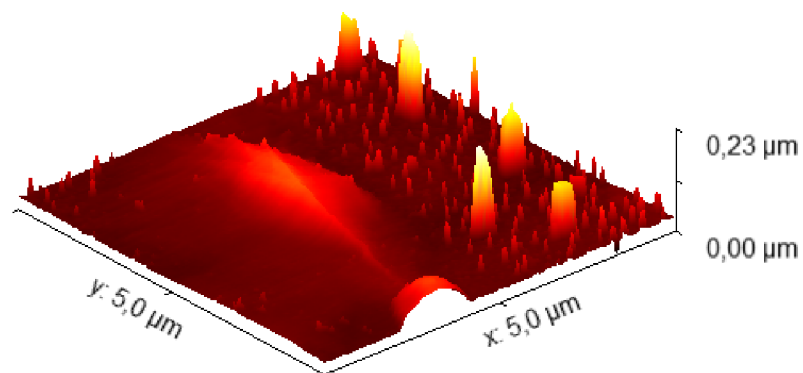

Figure 4.14: AFM image of the fabricated structure. Image was done by Radek Dao.
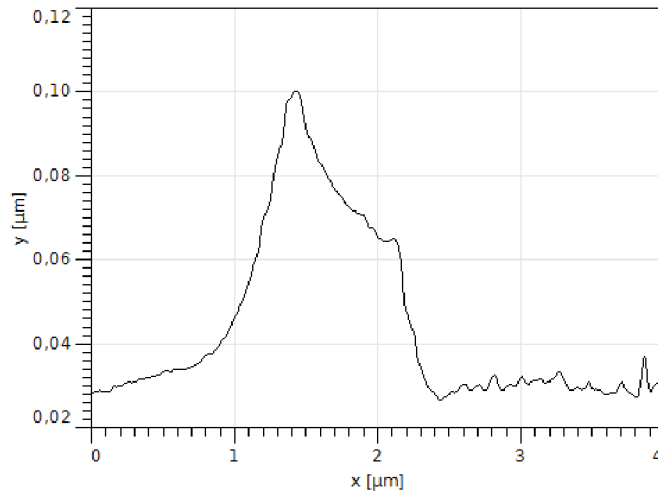
Figure 4.15: Cross-section profile of the fabricated structure at the highest point of the structure.

It is clear that this structure is not ideal, however, it serves as proof of concept, that indeed the combination of VLS growth and electron beam induced AuGe island migration can lead to the controlled fabrication of nanostructures.

Naturally, it will require much more experiments, optimization, and generally work to fully unlock the potential of this newly developed fabrication method. Many more experiments were planned with this method, however, they could not be done due to the Covid-19 restrictions.

Chapter 5

Conclusion

In the first part of the thesis, a study of electron beam induced migration of liquid metallic islands (AuGe islands) was presented. Simulations were done in Casino and Comsol software and showed how does the temperature field changes in the presence of the electron beam. In the experiments, it was possible to observe and manipulate islands in real-time. By combining simulation results with the experiments it was possible to determine that the temperature difference between the borders of the island is independent of the electron beam power and on the other hand it is dependent on the size of the islands. These results are in agreement with the predicted model. Based on the results of this work and [2] it is clear that the temperature gradient induced by the electron beam is responsible for the migration of islands.

The second part consisted of the ideas on how to utilize this controlled island manipulation for something practical. It was decided that the idea of 3-D micro/nano printing will be tested. This method employs the combination of island migration together with the VLS growth method which in an ideal case should work similarly to the well known 3-D printing. After the trial and error approach, I was able to grow a structure trough this combination of methods. The structure was very simple and could be hardly called a product of „3-D micro-printing", however it serves as a proof of concept and with more work could be improved into a real nano/micro-fabrication method.

Hopefully, will this work serve as a starting point for more work as I believe the topic itself holds much more potential in further applications than just ideas that were presented here.

Bibliography

[1] ASHKIN, A., DZIEDZIC, J. M., BJORKHOLM, J. and CHU, S. Observation of a single-beam gradient force optical trap for dielectric particles. *Optics letters*. Optical Society of America. 1986, vol. 11, no. 5, p. 288–290.

[2] ICHINOKAWA, T., HAGINOYA, C., INOUE, D., ITOH, H. and KIRSCHNER, J. Electro-and thermomigration of metallic islands on Si (100) surface. *Japanese journal of applied physics*. IOP Publishing. 1993, vol. 32, 3S, p. 1379.

[3] VOLKERT, C. Electromigration. In: BUSCHOW, K. J., CAHN, R. W., FLEMINGS, M. C., ILSCHNER, B., KRAMER, E. J. et al., ed. *Encyclopedia of Materials: Science and Technology*. Oxford: Elsevier, 2001, p. 2548 – 2556. Available at: `http://www.sciencedirect.com/science/article/pii/B0080431526004629`. ISBN 978-0-08-043152-9.

[4] HUNTINGTON, H. Electromigration in metals. *Diffusion in solids: recent developments*. Academic Press New York. 1975, p. 303–352.

[5] ALLNATT, A. R. and LIDIARD, A. B. *Atomic transport in solids*. Cambridge University Press, 2003.

[6] ZHAO, C., FU, J., OZTEKIN, A. and CHENG, X. Measuring the Soret coefficient of nanoparticles in a dilute suspension. *Journal of nanoparticle research*. Springer. 2014, vol. 16, no. 10, p. 2625.

[7] WILLIS MOCK, J. Thermomigration of Au 195 and Sb 125 in gold. *Physical Review*. APS. 1969, vol. 179, no. 3, p. 663.

[8] SHAO, T., CHEN, Y., CHIU, S. and CHEN, C. Electromigration failure mechanisms for SnAg 3.5 solder bumps on Ti/ Cr-Cu/ Cu and Ni (P)/ Au metallization pads. *Journal of applied physics*. American Institute of Physics. 2004, vol. 96, no. 8, p. 4518–4524.

[9] CHEN, C., HSIAO, H.-Y., CHANG, Y.-W., OUYANG, F. and TU, K. Thermomigration in solder joints. *Materials Science and Engineering: R: Reports*. Elsevier. 2012, vol. 73, 9-10, p. 85–100.

[10] DE GROOT, S. R. *Thermodynamics of irreversible processes*. North-Holland Amsterdam, 1951.

[11] ORIANI, R. Thermomigration in solid metals. *Journal of Physics and Chemistry of Solids.* Elsevier. 1969, vol. 30, no. 2, p. 339–351.

[12] ANTHONY, T. and CLINE, H. Thermal migration of liquid droplets through solids. *Journal of Applied Physics.* American Institute of Physics. 1971, vol. 42, no. 9, p. 3380–3387.

[13] ANTHONY, T. and CLINE, H. Random walk of liquid droplets migrating in silicon. *Journal of Applied Physics.* American Institute of Physics. 1976, vol. 47, no. 6, p. 2316–2324.

[14] MASSALSKI, T. B., OKAMOTO, H., SUBRAMANIAN, P., KACPRZAK, L. and SCOTT, W. W. *Binary alloy phase diagrams.* American Society for Metals Metals Park, OH, 1986.

[15] ANTHONY, T. and CLINE, H. Thermomigration of Gold-Rich Droplets in Silicon. *Journal of Applied Physics.* American Institute of Physics. 1972, vol. 43, no. 5, p. 2473–2476.

[16] ANTHONY, T. and CLINE, H. The kinetics of droplet migration in solids in an accelerational field. *Philosophical Magazine.* Taylor & Francis. 1970, vol. 22, no. 179, p. 0893–0901.

[17] DEMIREL, Y. and GERBAUD, V. Chapter 9 - Coupled Systems of Chemical Reactions and Transport Processes. In: DEMIREL, Y. and GERBAUD, V., ed. *Nonequilibrium Thermodynamics (Fourth Edition).* Fourth Editionth ed. Elsevier, 2019, p. 413 – 452. Available at: `http://www.sciencedirect.com/science/article/pii/B9780444641120000095`. ISBN 978-0-444-64112-0.

[18] CLINE, H. and ANTHONY, T. The thermomigration of liquid droplets through grain boundaries in solids. *Acta Metallurgica.* Elsevier. 1971, vol. 19, no. 6, p. 491–495.

[19] BOUASSE, H. *Capillarite: phenomenes superficiels.* Delagrave, 1924.

[20] BROCHARD, F. Motions of droplets on solid surfaces induced by chemical or thermal gradients. *Langmuir.* ACS Publications. 1989, vol. 5, no. 2, p. 432–438.

[21] BRZOSKA, J., BROCHARD WYART, F. and RONDELEZ, F. Motions of droplets on hydrophobic model surfaces induced by thermal gradients. *Langmuir.* ACS Publications. 1993, vol. 9, no. 8, p. 2220–2224.

[22] CHAUDHURY, M. K. and WHITESIDES, G. M. How to make water run uphill. *Science.* American Association for the Advancement of Science. 1992, vol. 256, no. 5063, p. 1539–1541.

[23] ZHU, X., WANG, H., LIAO, Q., DING, Y. and GU, Y. Experiments and analysis on self-motion behaviors of liquid droplets on gradient surfaces. *Experimental Thermal and Fluid Science.* Elsevier. 2009, vol. 33, no. 6, p. 947–954.

[24] MARANGONI, C. *Sull'espansione delle goccie d'un liquido galleggianti sulla superfice di altro liquido.* 1865.

[25] CHANDRASEKHAR, S. *Hydrodynamic and hydromagnetic stability.* Courier Corporation, 2013.

[26] DE GENNES, P.-G. Wetting: statics and dynamics. *Reviews of modern physics.* APS. 1985, vol. 57, no. 3, p. 827.

[27] BATCHELOR, C. K. and BATCHELOR, G. *An introduction to fluid dynamics.* Cambridge university press, 2000.

[28] ŠTUBIAN, M. *Studium katalitycké dekompozice oxidu křemičitého.* Brno, 2018. Bachelor's thesis. Brno University of Technology, Faculty of mechanical engineering. Supervisor Ing. Petr Bábor, Ph.D.

[29] *Comsol Multiphysics® 5.1.* Available at: www.comsol.com.

[30] ALLEN, F. Emissivity at 0.65 micron of silicon and germanium at high temperatures. *Journal of Applied Physics.* American Institute of Physics. 1957, vol. 28, no. 12, p. 1510–1511.

[31] DAO, R. *Modifikace povrchu nanokapkami ovládanými elektronovou pinzetou.* Brno, 2020. Master's thesis. Brno University of Technology, Faculty of mechanical engineering. Supervisor Ing. Petr Bábor, Ph.D.

[32] HOVONGTON, P. and DROUIN, D. *Casino 2.5.1.0.* Available at: https://www.gel.usherbrooke.ca/casino/index.html.

[33] REIMER, L. *Scanning electron microscopy: physics of image formation and microanalysis.* Springer, 2013.

[34] WAGNER, R. and ELLIS, W. Vapor-liquid-solid mechanism of single crystal growth. *Applied physics letters.* American Institute of Physics. 1964, vol. 4, no. 5, p. 89–90.

[35] RODRIGUES, V., FUHRER, T. and UGARTE, D. Signature of atomic structure in the quantum conductance of gold nanowires. *Physical review letters.* APS. 2000, vol. 85, no. 19, p. 4124.

[36] CHOI, H.-J. et al. Semiconductor nanostructures for optoelectronic devices. *NanoScience and Technology.* 2012.

[37] MONGILLO, M., SPATHIS, P., KATSAROS, G., GENTILE, P. and DE FRANCESCHI, S. Multifunctional devices and logic gates with undoped silicon nanowires. *Nano letters.* ACS Publications. 2012, vol. 12, no. 6, p. 3074–3079.

[38] YAN, R., GARGAS, D. and YANG, P. Nanowire photonics. *Nature photonics.* Nature Publishing Group. 2009, vol. 3, no. 10, p. 569–576.

[39] Shkondin, E., Alimadadi, H., Takayama, O., Jensen, F. and Lavrinenko, A. V. Fabrication of hollow coaxial Al2O3/ZnAl2O4 high aspect ratio freestanding nanotubes based on the Kirkendall effect. *Journal of Vacuum Science & Technology A: Vacuum, Surfaces, and Films.* American Vacuum Society. 2020, vol. 38, no. 1, p. 013402.

[40] Givargizov, E. Fundamental aspects of VLS growth. In: *Vapour Growth and Epitaxy.* Elsevier, 1975, p. 20–30.

[41] Wu, Y. and Yang, P. Direct observation of vapor- liquid- solid nanowire growth. *Journal of the American Chemical Society.* ACS Publications. 2001, vol. 123, no. 13, p. 3165–3166.

[42] Ross, F., Tersoff, J. and Reuter, M. Sawtooth faceting in silicon nanowires. *Physical review letters.* APS. 2005, vol. 95, no. 14, p. 146104.

[43] Sutter, E. A. and Sutter, P. W. Size-dependent phase diagram of nanoscale alloy drops used in vapor- liquid- solid growth of semiconductor nanowires. *ACS nano.* ACS Publications. 2010, vol. 4, no. 8, p. 4943–4947.